

THE MASSIVE HOSTS OF RADIO GALAXIES ACROSS COSMIC TIME

NICK SEYMOUR,¹ DANIEL STERN,² CARLOS DE BREUCK,³ JOEL VERNET,³ ALESSANDRO RETTURA,⁴ MARK DICKINSON,⁵
 ARJUN DEY,⁶ PETER EISENHARDT,² ROBERT FOSBURY,³ MARK LACY,¹ PAT MCCARTHY,⁶ GEORGE MILEY,⁷
 BRIGITTE ROCCA-VOLMERANGE,⁸ HUUB RÖTTGERING,⁹ S. ADAM STANFORD,^{10,11} HARRY TEPLITZ,¹
 WIL VAN BREUGEL,^{10,11} AND ANDREW ZIRM⁴

Received 2007 January 2; accepted 2007 March 2

ABSTRACT

We present the results of a comprehensive *Spitzer* survey of 69 radio galaxies across $1 < z < 5.2$. Using IRAC (3.6–8.0 μm), IRS (16 μm), and MIPS (24–160 μm) imaging, we decompose the rest-frame optical to infrared spectral energy distributions into stellar, AGN, and dust components and determine the contribution of host galaxy stellar emission at rest-frame *H*-band. Stellar masses derived from rest-frame near-IR data, where AGN and young star contributions are minimized, are significantly more reliable than those derived from rest-frame optical and UV data. We find that the fraction of emitted light at rest-frame *H* band from stars is $>60\%$ for $\sim 75\%$ of the high-redshift radio galaxies. As expected from unified models of AGNs, the stellar fraction of the rest-frame *H*-band luminosity has no correlation with redshift, radio luminosity, or rest-frame mid-IR (5 μm) luminosity. In addition, while the *stellar H*-band luminosity does not vary with stellar fraction, the *total H*-band luminosity anticorrelates with the stellar fraction as would be expected if the underlying hosts of these radio galaxies comprise a homogeneous population. The resultant stellar luminosities imply stellar masses of $10^{11} - 10^{11.5} M_{\odot}$ even at the highest redshifts. Powerful radio galaxies tend to lie in a similar region of mid-IR color-color space as unobscured AGNs, despite the stellar contribution to their mid-IR SEDs at shorter wavelengths. The mid-IR luminosities alone classify most HzRGs as LIRGs or ULIRGs with even higher total-IR luminosities. As expected, these exceptionally high mid-IR luminosities are consistent with an obscured, highly accreting AGN. We find a weak correlation of stellar mass with radio luminosity.

Subject headings: galaxies: active — galaxies: evolution — galaxies: high-redshift

Online material: color figures

1. INTRODUCTION

Luminous radio galaxies were the first class of obscured, or *type 2*, quasars to be discovered and characterized. They have accreting supermassive black holes whose continuum emission at UV, optical, and soft X-ray energies is absorbed by dust, thus allowing a *clear* view of the host galaxy. More recently, hard X-ray and mid-IR surveys have identified the radio-quiet cousins to luminous radio galaxies (e.g., Norman et al. 2002; Stern et al. 2002; Martínez-Sansigre et al. 2005; Polletta et al. 2006; Lacy et al. 2007). The main evidence that radio galaxies host supermassive black holes comes from the high luminosities of their radio lobes, which are fed by radio jets originating at the host galactic nuclei. The lobe spatial extents (up to a few Mpc; Saripalli et al. 2005) and luminosities ($L_{1.4\text{ GHz}} \geq 10^{25} \text{ W Hz}^{-1}$) clearly rule out a stellar origin for their energetics (e.g., Rees 1978). In terms of the orientation unification scheme for active galactic

nuclei (AGN) (e.g., Barthel 1989; Antonucci 1993; Urry & Padovani 1995), radio galaxies are radio-loud quasars seen from an angle where an optically thick torus obscures emission from the region closest to the central engine.

Due to their large radio luminosities, radio galaxies were the predominant way to probe the distant universe until the advent of 8–10 m class telescopes and the Lyman-break technique in the last decade. In fact, radio galaxies were the first galaxies to be found above redshifts one, two, three, and four (see Stern & Spinrad 1999 and references therein). Across cosmic time, the host galaxies of powerful radio sources appear to be uniquely robust indicators of the most massive galaxies in the universe. At low redshift, this result has been known since the first optical identifications of extragalactic radio sources showed them to be associated with massive, giant elliptical (gE and cD) galaxies (Matthews et al. 1964). In the more distant universe, indirect evidence that this association remains intact comes from the detection of host galaxies with $r^{1/4}$ law light profiles in *Hubble Space Telescope* (*HST*) observations of high-redshift radio galaxies (HzRGs) at $1 \lesssim z \lesssim 2$ (Pentericci et al. 2001; Waddington et al. 2002; Zirm et al. 2003; A. J. Bunker et al. 2007, in preparation); the tendency for HzRGs to reside in moderately rich (proto-) cluster environments (Le Fèvre et al. 1996; Pascarelle et al. 1996; Venemans et al. 2002, 2003, 2004, 2005, 2007; Stern et al. 2003); the spectacular ($>100 \text{ kpc}$) luminous $\text{Ly}\alpha$ halos seen around several sources, implying large gas reservoirs (Reuland et al. 2003; Villar-Martín et al. 2003); submillimeter detections of HzRGs, implying violent star formation activity up to $\sim 1000 M_{\odot} \text{ yr}^{-1}$ (Archibald et al. 2001; Reuland et al. 2004); and a few direct kinematic measurements of HzRGs (Dey et al. 1996; Dey & Spinrad 1996; Nesvadba et al. 2006). The most compelling evidence of this association of

¹ *Spitzer* Science Center, California Institute of Technology, 1200 East California Boulevard, Pasadena, CA 91125; seymour@ipac.caltech.edu.

² Jet Propulsion Laboratory, California Institute of Technology, Pasadena, CA 91109.

³ European Southern Observatory, Karl Schwarzschild Straße, D-85748 Garching, Germany.

⁴ Johns Hopkins University, 3400 North Charles Street, Baltimore, MD 21218.

⁵ National Optical Astronomy Observatory, Tucson, AZ 85719.

⁶ Carnegie Observatories, 813 Santa Barbara Street, Pasadena, CA 91101.

⁷ Leiden Observatory, University of Leiden, P.O. Box 9513, 2300 RA Leiden, Netherlands.

⁸ Institut d'Astrophysique de Paris, 98bis Bd Arago, 75014 Paris, France.

⁹ University of California, Davis, CA 95616.

¹⁰ Institute of Geophysics and Planetary Physics, Lawrence Livermore National Laboratory, Livermore, CA 94551.

¹¹ University of California, Merced, P.O. Box 2039, Merced, CA 95344.

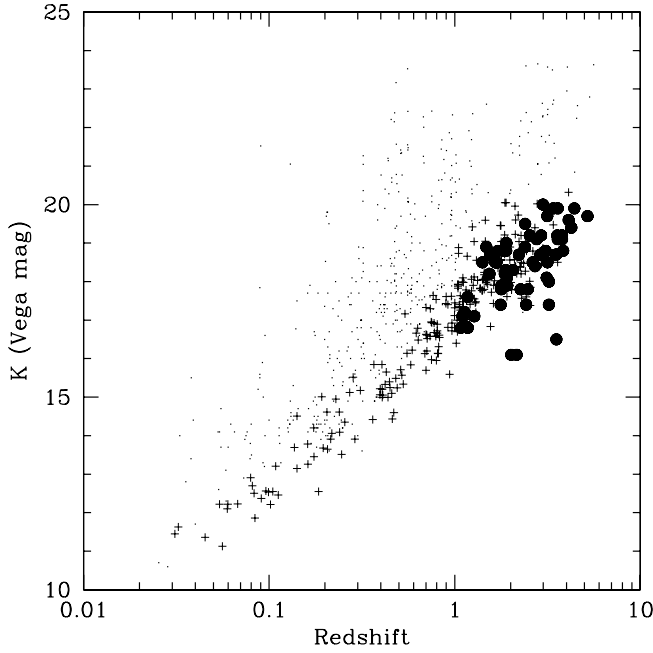


FIG. 1.—Hubble K - z diagram of radio-loud (pluses and filled circles) and radio-quiet galaxies (points). The radio-loud sample is from De Breuck et al. (2002). The radio quiet samples are from the Hawaii survey (Songaila et al. 1994) and the Hubble Deep Field–North (Dickinson et al. 2003). The filled circles indicate the 69 $z > 1$ radio galaxies that comprise our *Spitzer* sample. The three HzRGs falling below the obvious correlation are MRC 0156–252 ($z = 2.016$), PKS 1138–262 ($z = 2.156$), and TX J1908+7220 ($z = 3.530$). MRC 0156–252 is known to have strong $H\alpha$ in the K band (Eales & Rawlings 1996), and PKS 1138–262 has also recently been confirmed to have strong $H\alpha$ in the K band (Nesvadba et al. 2006). TX J1908+7220 has a strong unresolved AGN component (see notes in individual sources) and seems closer to being an unobscured quasar than a radio galaxy.

HzRGs with the most massive systems, however, is the tight correlation of the observed near-infrared Hubble, or K - z , diagram for powerful radio sources (Fig. 1; Lilly & Longair 1984; Best et al. 1998; Eales et al. 1997; van Breugel et al. 1998; Jarvis et al. 2001; De Breuck et al. 2002; Willott et al. 2003; Rocca-Volmerange et al. 2004; Brookes et al. 2006): HzRGs form a narrow redshift sequence that traces the envelope of radio-quiet galaxies and is well modeled by the evolution of a stellar population formed at high redshift from an accumulation of up to $10^{12} M_{\odot}$ of pregalactic baryonic material. The large-scale, double-lobed radio morphologies and enormous radio luminosities suggested early on that HzRGs must have spinning supermassive black holes powering relativistic jets in their centers (Rees 1978; Blandford & Payne 1982). With the more recent discovery that the stellar bulge and central black hole masses of galaxies are closely correlated (e.g., Tremaine et al. 2002), it is no longer a surprise that the parent galaxies of the most powerful radio sources occupy the upper end of the galaxy mass function.

Despite two decades of study since the initial discovery of the HzRG K - z relation (Lilly & Longair 1984), the nature and tightness of the relation remains mysterious. The scatter in the relation is surprisingly low out to $z \sim 1$, and only increases modestly at higher redshifts as the observed K -band samples rest-frame optical emission (e.g., Fig. 1; De Breuck et al. 2002). Interpretations have generally relied on these observed near-IR observations probing the stellar populations of the distant radio galaxies (e.g., Rocca-Volmerange et al. 2004). However, detailed interpretations have been complicated by (1) uncertain contributions of AGN-related light, which are most important in the rest-frame UV (e.g., Vernet et al. 2001), (2) evolution of the host galaxy stel-

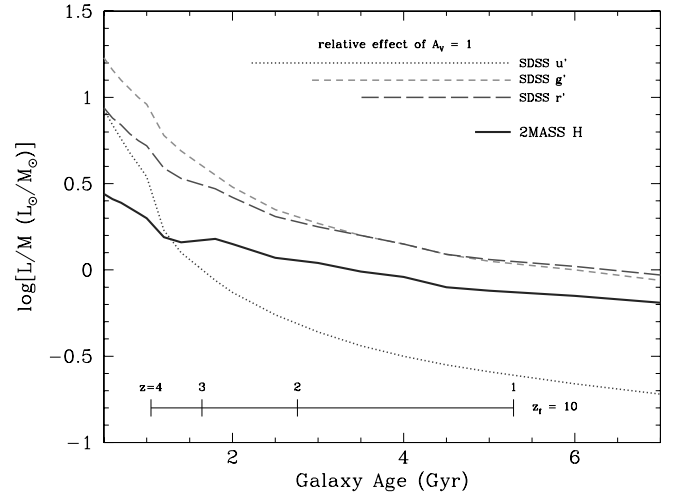


FIG. 2.—Light-to-mass ratios (in solar units) as a function of age for the adopted PEGASE.2 elliptical galaxy model for different rest-frame optical (SDSS u' , g' , r') and near-IR (2MASS H) passbands. The light-to-mass ratio for the H -band filter, near the peak of stellar emission, varies much less as a function of age than the shorter wavelength filters. In addition, the optical passbands are more susceptible to (1) dust absorption—the relative effects of 1 mag of visual extinction in each of the passbands is illustrated by the horizontal lines; in units of A_V , H band is more than 4 times less sensitive to dust extinction than r' , (2) uncertainty in the age of the stellar population, and (3) the addition of light from a second, younger population. For a formation redshift of $z_{\text{form}} = 10$, the corresponding ages are marked near the bottom of the figure for different redshifts. For $z_{\text{form}} = 14$ or 7, the tracks shift 0.2 Gyr to the left or 0.3 Gyr to the right, respectively. As the H -band track is fairly flat, this uncertain formation redshift has little effect on our derived light-to-mass ratio. [See the electronic edition of the Supplement for a color version of this figure.]

lar population(s), and (3) band-shifting, meaning that observed $2.2 \mu\text{m}$ samples very different emitting wavelengths for different redshift sources, reaching into the rest-frame ultraviolet for the most distant HzRGs.

In this paper, we present observations of a large sample of HzRGs obtained with the *Spitzer Space Telescope* (Werner et al. 2004). By observing the same rest-frame near- to mid-IR spectral range for sources over a large redshift range ($1 < z < 5.2$), we remove many of the complications that plagued previous studies. In particular, the $1.6 \mu\text{m}$ peak of the stellar emission provides a reasonably robust measure of the stellar mass for stellar populations with ages ≥ 1 Gyr (Sawicki 2002). While UV and optical emission has strong contributions from the youngest and hottest stars in a galaxy, near-IR emission primarily derives from the low-mass stars that dominate the stellar mass of a galaxy. Thus, while rest-frame UV and optical studies of galaxies are well-suited to probe galaxy star-formation rates, rest-frame near-IR studies are well-suited to probe galaxy stellar masses. We discuss this approach and other recent results that might affect it (e.g., Maraston 2005) in detail in § 6.

Figure 2 illustrates the advantage of rest-frame near-IR derivations of stellar masses. First, the impact of dust extinction falls sharply with wavelength, making quantities derived from rest-frame near-IR observations more than an order of magnitude less susceptible to uncertain dust extinction corrections relative to optical observations. Second, since the main-sequence lifetimes of low-mass stars exceed the Hubble time, galaxy masses derived from rest-frame near-IR observations are relatively insensitive to the age of stellar populations or the star formation history. In particular, secondary bursts of star formation will affect UV and optical magnitudes significantly more than near-IR magnitudes.

We here use mid-IR observations of a large sample of radio galaxies to probe their host galaxy stellar masses. By observing

consistently on both sides of the $1.6\ \mu\text{m}$ peak of the stellar emission, we avoid complicated k -correction effects and derive a reasonably robust measure of the stellar mass for stellar populations with ages $\gtrsim 1$ Gyr. Observations at longer wavelengths allow us to determine the contribution of warm, AGN-heated dust emission to the rest-frame near-IR emission. Our paper is organized as follows. Section 2 describes the *Spitzer* HzRG sample. Section 3 presents the *Spitzer* mid- to far-IR data and their reduction. Section 4 describes our χ^2 fitting of the spectral energy distributions (SEDs), and § 5 presents the results of this fitting. Section 6 describes how the derived rest-frame H -band luminosities are converted into stellar masses. Section 7 discusses and concludes this analysis. We present notes on individual sources as an Appendix. This paper presents our entire *Spitzer* data set and analyzes the bulk properties of the sample. *Spitzer* observations of individual sources from this program have been the subject of detailed studies by Villar-Martín et al. (2006) of MRC 2104–242 at $z = 2.49$, by Stern et al. (2006) of LBDS 53W091 at $z = 1.55$, by Broderick et al. (2007) of PKS at $z = 2.156$, and by C. De Breuck et al. (2007, in preparation) of 4C 23.56 at $z = 2.48$.

Throughout we assume a concordance model¹² of universe expansion, $\Omega_M = 1 - \Omega_\Lambda = 0.3$, $\Omega_0 = 1$, and $H_0 = 70\ \text{km s}^{-1}\text{Mpc}^{-1}$. Inferred luminosities presented in this paper are of the form $\nu L_\nu/L_\odot$, where $L_\odot = 3.9 \times 10^{23}\ \text{W}$.

2. THE SPITZER HIGH-REDSHIFT RADIO GALAXY SAMPLE

Our HzRG sample is drawn from radio galaxy surveys executed during the last 45 years (starting with the 3CR; Bennett 1962). We have searched both flux-limited surveys such as the 3C (Spinrad et al. 1985), 6CE (Eales et al. 1997), 7C (Lacy et al. 1999; Willott et al. 2001), MG (Bennett et al. 1986; Lawrence et al. 1986), and MRC (McCarthy et al. 1996), as well as surveys filtered by their ultrastep radio spectra (USS; e.g., Chambers et al. 1996; Röttgering et al. 1997; De Breuck et al. 2001). The former provide a sample unbiased in their radio properties but lack the high-redshift ($z > 2$) sources mainly found in the USS samples. Because the USS samples also probe fainter radio flux densities, including such sources allows us to break the strong luminosity–redshift degeneracy of flux density-limited surveys.

For the purposes of this work we define a HzRG as a radio galaxy above a redshift of one with a rest-frame 3 GHz luminosity greater than $10^{26}\ \text{W Hz}^{-1}$. This choice is to ensure that we include only those objects with very powerful obscured AGNs. This value is similar to that used by other authors to separate AGNs based on their radio luminosities. The classical luminosity that separates Fanaroff & Riley (1974) type 1 and type 2 sources (which are morphologically distinct), converted from 178 MHz to 3 GHz, is $10^{25.4}$ ($10^{24.8}$) W Hz^{-1} assuming a steep (ultrastep) radio spectral index of $\alpha = -0.8$ (-1.3). A more recent radio-loud/radio-quiet division is $L_{3\text{GHz}} = 10^{26.3}$ ($10^{26.4}$) W Hz^{-1} (Miller et al. 1990) and an upper limit to radio-quiet QSOs of $L_{3\text{GHz}} = 10^{25.2}$ ($10^{25.1}$) W Hz^{-1} was found by Gregg et al. (1996) both converted to 3 GHz luminosity assuming the same spectral index values.

To examine how *Spitzer*-derived quantities depend on redshift and radio luminosity, we selected a representative subset of

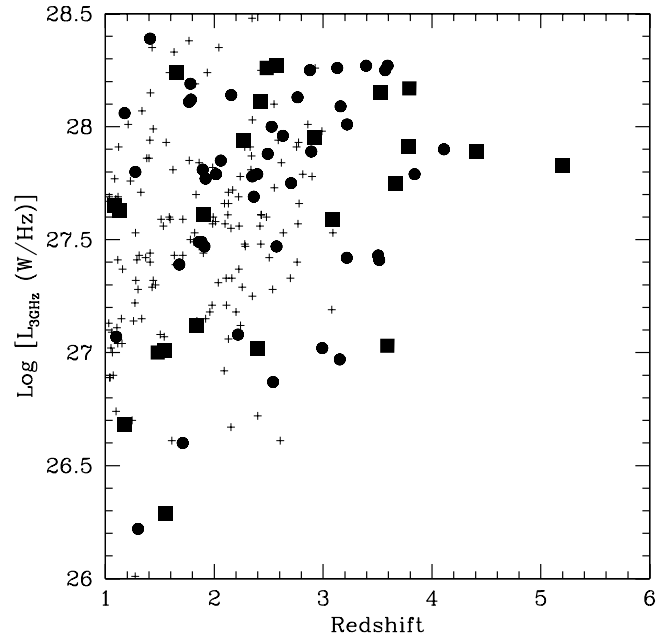


FIG. 3.—Radio luminosity at rest-frame 3 GHz plotted against redshift for 263 $z > 1$ radio galaxies from the literature (pluses). Filled symbols indicate sources in our *Spitzer* program, carefully chosen to uniformly cover 1.5–2 orders of magnitude in radio power at each redshift $1 < z < 4$. The entire *Spitzer* sample was observed with IRAC. Radio galaxies at $z > 2$ were imaged at $16\ \mu\text{m}$ with IRS. Radio galaxies in “low” Galactic infrared background (see § 3) are indicated as solid squares and were observed with MIPS.

69 targets from the parent sample of 263 known $z > 1$ HzRGs (circa 2003; Fig. 3). Table 1 lists the selected subset, which spans the full range of redshifts from $z = 1$ to the redshift of the most distant known radio galaxy, TN J0924–2201 at $z = 5.19$ (van Breugel et al. 1999). Most sources were observed as part of *Spitzer* Cycle 1 (Program ID number 3329); a few observations derive from guaranteed time observations by *Spitzer* instrument teams. We required at least 15 sources in each $\Delta z = 1$ bin, covering a range of rest-frame 3 GHz radio luminosity, $L_{3\text{GHz}}$. To obtain a uniform set of radio luminosities of a sample of radio galaxies covering the entire sky, we obtained radio flux densities from the largest all-sky radio surveys, i.e., the 1.4 GHz NRAO VLA Sky Survey (NVSS; Condon et al. 1998), the 325/352 MHz Westerbork Northern Sky Survey (WENSS; Rengelink et al. 1997), and the 365 MHz Texas Survey (Douglas et al. 1996). These surveys all have $\sim 1'$ spatial resolution, which has the advantage that the entire sample appear essentially as point sources, thereby minimizing issues of missing flux from overresolved emission. We chose 3 GHz as the fiducial rest frequency as it is the midpoint between the survey frequencies at the median redshift of our sample. This choice ensures that almost all radio luminosities are interpolated, rather than extrapolated as is often required when deriving lower rest frequency luminosities (e.g., 151 or 178 MHz). Blundell et al. (1998) argue, however, that low-frequency luminosities are a better measure of the total radio luminosity, as the emission at low frequency is dominated by the steep-spectrum, isotropic radio lobes, while high-frequency emission may be contaminated by Doppler-boosted emission from flat-spectrum radio cores. Until the completion of all-sky < 100 MHz surveys, such low-frequency rest-frame luminosities cannot be uniformly derived for our sample. However, most HzRGs in our sample have weak radio cores, which although flatter than the ultrastep-spectrum radio lobes, still have steep radio spectra (e.g., Athreya et al. 1997) and thus are not expected to significantly boost the rest-frame 3 GHz luminosity.

¹² These common values of the “concordance” cosmology underestimate luminosities (and hence stellar masses) by $\sim 2\%$ – 3% at $z = 3$ – 4 when compared to the latest *Wilkinson Microwave Anisotropy Probe* measurements, $\Omega_M = 1 - \Omega_\Lambda = 0.25$, $\Omega_0 = 1$, and $H_0 = 73\ \text{km s}^{-1}\text{Mpc}^{-1}$ (Spergel et al. 2007). Lower redshift HzRGs show an even smaller systematic adjustment, implying that the assumed cosmological parameters are inconsequential to our analysis.

TABLE 1
Spitzer HzRG SAMPLE AND EXPOSURE TIMES PER INSTRUMENT

HzRG	R.A. (J2000.0)	Decl. (J2000.0)	Redshift	$\log(L_{3\text{ GHz}})$ (W Hz ⁻¹)	<i>K</i> Band ^a (Vega)	IRAC Exp. Time (s)	IRS Exp. Time (s)	MIPS Exp. Time (s)
6C 0032+412.....	00 34 53.1	41 31 31.50	3.670	27.75	19.10	120	122	134, 420, 881
MRC 0037-258.....	00 39 56.4	-25 34 31.01	1.100	27.07	17.10	120
6C* 0058+495.....	01 01 18.9	49 50 12.29	1.173	26.68	17.60	120	...	134, 420, 881
MRC 0114-211.....	01 16 51.4	-20 52 06.71	1.410	28.39	18.50	120
TN J0121+1320.....	01 21 42.7	13 20 58.00	3.516	27.41	18.70	120	122	...
6C* 0132+330.....	01 35 30.4	33 17 00.82	1.710	26.60	18.80	120
6C 0140+326.....	01 43 43.8	32 53 49.31	4.413	27.89	19.90	5000	122	267, 671, 2643
MRC 0152-209.....	01 54 55.8	-20 40 26.30	1.920	27.77	17.90	120
MRC 0156-252.....	01 58 33.6	-24 59 31.10	2.016	27.79	16.10	120	122	...
TN J0205+2242.....	02 05 10.7	22 42 50.40	3.506	27.43	18.70	120	122	...
MRC 0211-256.....	02 13 30.5	-25 25 21.00	1.300	26.22	...	120	122	...
3C 65.....	02 23 43.2	40 00 52.40	1.176	28.06	16.80	120
MRC 0251-273.....	02 53 16.7	-27 09 13.03	3.160	28.09	18.50	120	122	...
MRC 0316-257.....	03 18 12.0	-25 35 11.00	3.130	28.26	18.10	120	122	...
MRC 0324-228.....	03 27 04.4	-22 39 42.60	1.894	27.81	18.80	120
MRC 0350-279.....	03 52 51.6	-27 49 22.61	1.900	27.61	19.00	120	...	134, 420, 881
MRC 0406-244.....	04 08 51.5	-24 18 16.39	2.427	28.11	17.40	120	122	134, 420, 881
4C 60.07.....	05 12 54.8	60 30 52.01	3.788	27.91	19.20	120	122	134, 420, 881
PKS 0529-549.....	05 30 25.2	-54 54 22.00	2.575	28.27	...	120	122	134, 420, 881
WN J0617+5012.....	06 17 39.4	50 12 55.40	3.153	26.97	19.70	120	122	...
4C 41.17.....	06 50 52.1	41 30 31.00	3.792	28.17	19.10	5000	122	267, 671, 2643
WN J0747+3654.....	07 47 29.4	36 54 38.09	2.992	27.02	20.00	120	122	...
6CE 0820+3642.....	08 23 48.1	36 32 46.42	1.860	27.49	18.20	120
USS 0828+193.....	08 30 53.4	19 13 16.00	2.572	27.47	18.20	120	122	...
5C 7.269.....	08 28 38.8	25 28 27.10	2.218	27.08	18.90	120	122	...
6CE 0901+3551.....	09 04 32.4	35 39 03.23	1.910	27.47	18.10	120
6CE 0905+3955.....	09 08 16.9	39 43 26.00	1.883	27.49	18.30	120
B2 0902+34.....	09 05 30.1	34 07 56.89	3.395	28.27	19.90	1200	122	2557, 2696, 3556
TN J0924-2201.....	09 24 19.9	-22 01 41.00	5.195	27.83	19.70	120	122	134, 420, 881
6C 0930+389.....	09 33 06.9	38 41 50.14	2.395	27.79	19.50	120	122	...
USS 0943-242.....	09 45 32.7	-24 28 49.65	2.923	27.95	19.20	120	122	134, 420, 881
3C 239.....	10 11 45.4	46 28 19.75	1.781	28.19	17.80	120
MRC 1017-220.....	10 19 49.0	-22 19 58.03	1.768	28.11	17.40	120
MG 1019+0534.....	10 19 33.4	5 34 34.80	2.765	28.13	19.10	120	122	...
WN J1115+5016.....	11 15 06.9	50 16 23.92	2.540	26.87	19.20	120	122	...
3C 257.....	11 23 09.2	5 30 19.47	2.474	28.62	17.80	120	122	...
WN J1123+3141.....	11 23 55.9	31 41 26.14	3.217	27.42	17.40	120	122	...
PKS 1138-262.....	11 40 48.6	-26 29 08.50	2.156	28.14	16.10	3000	122	9000, ..., ...
3C 266.....	11 45 43.4	49 46 08.24	1.275	27.80	17.10	120
6C 1232+39.....	12 35 04.8	39 25 38.91	3.220	28.01	18.00	120	122	...
USS 1243+036.....	12 45 38.4	3 23 20.70	3.570	28.25	19.20	120	122	...
TN J1338-1942.....	13 38 26.0	-19 42 31.00	4.110	27.90	19.60	5000	122	...
4C 24.28.....	13 48 14.8	24 15 52.00	2.879	28.25	...	120	122	...
3C 294.0.....	14 06 44.0	34 11 25.00	1.786	28.12	17.90	120
USS 1410-001.....	14 13 15.1	0 22 59.70	2.363	27.69	...	120	122	...
8C 1435+635.....	14 36 37.1	63 19 14.00	4.250	28.55	19.40	120	122	134, 420, 881
USS 1558-003.....	16 01 17.3	0 28 48.00	2.527	28.00	...	120	122	...
USS 1707+105.....	17 10 06.5	10 31 06.00	2.349	27.78	...	120	122	...
LBDS 53w002.....	17 14 14.7	50 15 29.70	2.393	27.02	18.90	3300	122	134, 420, 881
LBDS 53w091.....	17 22 32.7	50 06 01.94	1.552	26.29	18.70	900	...	633, 1311, 2643
3C 356.0.....	17 24 19.0	50 57 40.30	1.079	27.65	16.80	120	...	134, 420, 881
7C 1751+6809.....	17 50 49.9	68 08 25.93	1.540	27.01	18.20	120	...	134, 420, 881
7C 1756+6520.....	17 57 05.4	65 19 53.11	1.480	27.00	18.90	120	...	134, 420, 881
3C 368.0.....	18 05 06.3	11 01 33.00	1.132	27.63	17.20	120	...	134, 420, 881
7C 1805+6332.....	18 05 56.9	63 33 13.14	1.840	27.12	18.80	120	...	134, 420, 881
4C 40.36.....	18 10 55.7	40 45 24.01	2.265	27.94	17.80	120	122	134, 420, 881
TX J1908+7220.....	19 08 23.7	72 20 11.82	3.530	28.15	16.50	120	122	134, 420, 881
WN J1911+6342.....	19 11 49.6	63 42 09.60	3.590	27.03	19.90	120	122	134, 420, 881
TN J2007-1316.....	20 07 53.3	-13 16 43.62	3.840	27.79	18.80	120	122	...
MRC 2025-218.....	20 27 59.5	-21 40 56.90	2.630	27.96	18.50	120	122	...
MRC 2048-272.....	20 51 03.6	-27 03 02.53	2.060	27.85	18.30	120	122	...
MRC 2104-242.....	21 06 58.1	-24 05 11.00	2.491	27.88	...	120	122	...
4C 23.56.....	21 07 14.8	23 31 45.00	2.483	28.26	19.73	120	122	134, 420, 881
MG 2144+1928.....	21 44 07.5	19 29 14.60	3.592	28.27	19.10	120	122	...

TABLE 1—*Continued*

HzRG	R.A. (J2000.0)	Decl. (J2000.0)	Redshift	$\log(L_{3\text{ GHz}})$ (W Hz^{-1})	K Band ^a (Vega)	IRAC Exp. Time (s)	IRS Exp. Time (s)	MIPS Exp. Time (s)
USS 2202+128	22 05 14.1	13 05 33.50	2.706	27.75	18.40	120	122	...
MRC 2224–273	22 27 43.3	–27 05 01.71	1.679	27.39	18.50	120
B3 J2330+3927	23 30 24.9	39 27 12.02	3.086	27.59	18.80	120	122	134, 420, 881
4C 28.58	23 51 59.2	29 10 28.99	2.891	27.89	18.70	120	122	...
3C 470	23 58 35.3	44 04 38.87	1.653	28.24	18.50	120	...	134, 420, 881

NOTE.—Units of right ascension are hours, minutes, and seconds, and units of declination are degrees, arcminutes, and arcseconds.

^a K -band magnitude within projected 64 kpc radius.

We have preferentially selected sources with the most supporting data. Forty-seven of the 69 HzRGs in our sample have *HST* data, representing over 1.5 Ms of *HST* time. We also preferentially included sources previously selected for guaranteed time observations (GTOs) by the *Spitzer* instrument teams, thereby minimizing our *Spitzer* observatory request while maintaining a uniformly selected sample. Finally, we preferentially selected sources with millimeter and submillimeter observations in order to have information on the SEDs longward of the *Spitzer* coverage. Note that the sample does not suffer a bias toward cold dust properties as we select only on the basis of (sub-) millimeter observations, not detections.

3. INFRARED OBSERVATIONS AND REDUCTIONS

The *Spitzer* observations consist of imaging photometry in eight bands, using the entire instrument complement of the observatory. Data from the Infrared Array Camera (IRAC; Fazio et al. 2004) comes from all four bands (3.6, 4.5, 5.8, and 8 μm —synonymously referred to as channels 1, 2, 3, and 4). The entire sample of 69 HzRGs was observed with IRAC.¹³ Data from the Infrared Spectrograph (IRS; Houck et al. 2004) obtained in “peak-up imaging” mode (cf., Teplitz et al. 2005) provides flux densities at 16 μm for the 46 objects in our sample at $z > 2$. For the lower redshift portion of our sample, IRAC 8 μm images adequately cover the SED longward of the 1.6 μm stellar bump. Finally, the Multiband Imaging Photometer for *Spitzer* (MIPS; Rieke et al. 2004) was used to image a subset of our sample using all three available bands (24, 70, and 160 μm). Due to the uncertain ability of MIPS to image against the Galactic infrared background at the time of our GO Cycle 1 submission, only the 26 HzRGs from our sample lying in “low” background regions ($S_{24\text{ }\mu\text{m}} < 20\text{ MJy sr}^{-1}$) were observed with MIPS. Table 1 presents the 69 HzRGs comprising our sample, along with their coordinates, redshifts, rest-frame 3 GHz radio luminosities, 64 kpc K -band magnitudes (Vega), and which *Spitzer* instruments they have been observed with.

The 141 unique target/instrument observations comprising our survey were released from the *Spitzer* archive between 2004 October and 2006 June. Fourteen observations were part of the initial GTO programs (e.g., Stern et al. 2006). In general, our data reduction begins with the basic calibrated data (BCD) output of the *Spitzer* Science Center pipeline, using the most current version number at the time the data were initially released (e.g., S9 to S13). Improvements over the generations of pipelines implemented here were minor and did not warrant reprocessing data. The most useful augmentation was the addition of a global world coordinate system to the IRS peak-up images in S11. Note that

the units of *Spitzer* BCD images are in surface brightness units of MJy sr^{-1} , where 1 MJy sr^{-1} corresponds to $23.5\text{ }\mu\text{Jy arcsec}^{-2}$.

3.1. IRAC OBSERVATIONS

Most of the IRAC observations consisted of four dithered 30 s exposures in each of the four IRAC channels. For each channel, the BCDs were mosaicked using the MOPEX package (Makovoz & Khan 2005) from the *Spitzer* Science Center and resampled by a factor of 2 to give a pixel scale of $0.61''$. The MOPEX outlier (e.g., cosmic ray, bad pixel) rejection was optimized for the regions of deepest coverage in the center of the maps, corresponding to the location of the targeted HzRGs. The eight GTO IRAC observations were all deeper than our standardized program and were reduced in a similar manner with MOPEX. Source extraction was performed with SExtractor (Bertin & Arnouts 1996) in dual image mode, using the 3.6 μm channel for source detection. All IRAC BCD images have astrometry derived from 2MASS survey and are good to $<0.5''$, so we can be confident of the radio galaxy identifications.

We generally used the a $7''$ diameter aperture for photometry, although in a few cases where the source was faint and/or had a close companion, we extracted photometry using a $3.5''$ diameter aperture. The aperture corrections, applied after the conversion from surface brightness to flux density, are listed in Table 2 and are taken from the *Spitzer* First Look Survey (Lacy et al. 2005). The resulting flux densities are listed in Table 3 and include the total uncertainty in the IRAC photometry; i.e., the statistical uncertainties are added in quadrature to the systematic uncertainty of $\sim 10\%$. The systematic uncertainty is the total uncertainty from several different effects: the uncertainty in the IRAC flux density calibration, a flat-fielding color-dependent uncertainty, and variation of the PSF across the field of view. Nondetections have 3σ upper limits listed. The statistical uncertainties in the mosaicked images were calculated from the pixel-to-pixel rms from single BCDs (with the native pixel scale), converted to μJy , multiplied by the square root of the area of the aperture in square pixels, divided by the square root of the number of frames, and multiplied by the appropriate aperture correction. In all cases, the radio galaxies are well detected in the 3.6 and 4.5 μm channels.¹⁴ In most cases, the radio galaxies are also detected in the 5.8 and 8 μm channels. In no cases were the HzRGs resolved in channel 1, the highest resolution of all the *Spitzer* imaging bands with a PSF FWHM of $1.44''$.

3.2. IRS OBSERVATIONS

The IRS observations consisted of just two nodded exposures of the 16 μm peak-up imager, each of 61 s duration. The observations

¹³ Although 3C 65 was observed in only two bands due to an astrometric error in NED, which we have since had corrected.

¹⁴ 3C 65 is not observed in the 4.5 μm channel. 6C 0140+326 is probably detected at 3.6 and 4.5 μm but is blended by a foreground galaxy. Likewise 3C 294 is detected in all four channels, but the proximity of a bright star means only upper limits can be determined for channels at 3.6 and 4.5 μm .

TABLE 2
Spitzer PHOTOMETRIC PARAMETERS

Filter	Wavelength (μm)	Pixel Scale (arcsec pixel $^{-1}$)	Conv. to μJy	Aperture ^a (arcsec)	Annulus ^b (arcsec)	Aperture Correction
IRAC 1.....	3.6	0.61	23.5	3.5 7.0	9.76 9.76	1.48 1.13
IRAC 2.....	4.5	0.61	23.5	3.5 7.0	9.76 9.76	1.60 1.168
IRAC 3.....	5.8	0.61	23.5	3.5 7.0	9.76 9.76	2.76 1.155
IRAC 4.....	8.0	0.61	23.5	3.5 7.0	9.76 9.76	2.13 1.316
IRS-blue.....	16	1.2	0.591 ^c	6	6–10	...
MIPS 1.....	24	1.25	36.71	13	20–32	1.167
MIPS 2.....	70	4.95	576	35	39–65	1.211 ^d
MIPS 3.....	160	8	1500	50	75–125	1.445

^a Diameter at which the photometry is measured.

^b Inner and outer diameter of annulus used to determine the background sky level, except for the IRAC bands, where we provide the size of the background mesh used by SExtractor.

^c Including aperture correction.

^d For a power-law SED, $f_\nu \propto \nu^{-2}$.

were executed in *Spitzer* Cycle 1, before IRS “peak-up imaging” was offered as a supported observing mode. However, all the data were reduced with the more recent S13.2.0 version of the archive pipeline, which provides astrometry to the BCD products accurate to 0.5'' relative to the 2MASS reference frame. Subimages were made of just the blue (16 μm) “peak-up” field of view in which the radio galaxy was centered. Difference images were then created by subtracting one frame from the other, thereby removing background emission and latent patterns in the array.

The dithered difference images were then combined with bad pixels and flaring pixels masked. Flux densities were extracted with the IRAF DAOPHOT task using the parameters listed in Table 2. Random uncertainties were determined from the rms in each BCD and converted to μJy . The total uncertainties in this table include the random and the 7.8% (6% zero point uncertainty and 5% color correction) systematic uncertainties. The systematic and random uncertainties are combined in quadrature and used for the SED fitting discussed in § 4. These flux densities and uncertainties are listed in Table 3. Nondetections are represented by 3 σ upper limits. All 46 of the *Spitzer* HzRG sample at $z \geq 2$ were observed with IRS, as was MRC 0211–256 ($z = 1.300$) due to an error in the submitted AORs.¹⁵ We have robust 16 μm detections of the radio galaxy in 35 of the 47 observations.¹⁶

3.3. MIPS OBSERVATIONS

The MIPS observations were restricted to the 26 HzRGs with “low” mid-IR background ($S_{24\mu\text{m}} < 20 \text{ MJy sr}^{-1}$) and consisted of one cycle of 30 s exposures at 24 μm , three cycles of 10 s exposures at 70 μm , and five cycles of 10 s exposures at 160 μm . The 24 μm BCDs were median filtered to remove a regular stripe artifact pattern prior to mosaicking. Both the 24 and 70 μm data were then mosaicked with MOPEX using standard inputs and with the pixels resampled by a factor of 2. Twenty-two of the 24 μm observations resulted in detections, but only four radio galaxies are detected at 70 μm . None of our HzRG sample are detected at 160 μm . As we shall see below, the upper limits at long

wavelengths are still quite useful for constraining the mid-IR SED. Flux densities were extracted with the IRAF DAOPHOT task using the parameters listed in Table 2. For the 70 μm band we use an aperture correction based on a steep spectrum ($F_\lambda \propto \lambda^0$). Again, Table 3 provides flux densities and upper limits (3 σ) for all three MIPS cameras.

The random uncertainties (and 3 σ upper limits in Table 3) are derived from the BCDs and converted to μJy . The color correction can be quite significant for these broad MIPS bands that were calibrated using Galactic stars, e.g., typically for a Rayleigh-Jeans spectrum, $F_\lambda \propto \lambda^{-4}$. For the 70 and 160 μm bands we include a 5% systematic uncertainty to account for the uncertain color correction. For 24 μm we typically find that the SED is very nonstellar. As a first approximation, we apply the color correction by multiplying by 0.961 (from the MIPS data handbook¹⁷) for $\lambda F_\lambda = \text{constant}$, which approximates the observed SEDs of our HzRGs. We further include a 2% systematic uncertainty for the remaining unknown color correction. The final systematic uncertainties are 4.5%, 8.6%, and 13% for 24, 70, and 160 μm , respectively, including flux-calibration uncertainties from the *Spitzer* Observers Manual and color correction uncertainties described above. The systematic uncertainties are combined in quadrature with the statistical uncertainties and are presented in Table 3.

3.4. Mid-IR Colors of HzRGs

Recent work has shown that IRAC mid-IR colors reliably isolate spectroscopically confirmed, luminous, unobscured AGNs (e.g., Lacy et al. 2004; Stern et al. 2005). However, since the surface density of sources with mid-IR colors similar to unobscured AGNs is much higher than that of optically selected (type 1) quasars, it has been inferred that obscured, type 2 quasars are likewise identifiable from their mid-IR colors. Due to their optical faintness, type 2 quasars are not as well studied as their bright, type 1 cousins. However, they are a natural consequence of AGN unification schemes (e.g., Antonucci 1993), and models of the hard X-ray background imply that they outnumber type 1 quasars by factors of several (e.g., Treister et al. 2004).

Our *Spitzer* HzRG sample represents the largest sample of confirmed type 2 quasars with IRAC photometry obtained to date.

¹⁵ It was inadvertently confused with USS 0211–122 ($z = 2.336$).

¹⁶ Except for the nondetection of the highest redshift radio galaxy, TN J0924–2201 ($z = 5.195$), the 16 μm nondetections are evenly distributed across $z \sim 2$ –4.

¹⁷ See <http://ssc.spitzer.caltech.edu/mips/dh/mipsdatahandbook3.2.pdf>.

TABLE 3
Spitzer PHOTOMETRY FOR HzRGs (μJy)

HzRG	$f_{3.6\mu\text{m}}$	$f_{4.5\mu\text{m}}$	$f_{5.8\mu\text{m}}$	$f_{8.0\mu\text{m}}$	$f_{16\mu\text{m}}$	$f_{24\mu\text{m}}$	$f_{70\mu\text{m}}$	$f_{160\mu\text{m}}$
6C 0032+412.....	15.4 \pm 2.1	33.8 \pm 3.7	57.6 \pm 8.9	98.3 \pm 10.0	205.0 \pm 34.9	457.0 \pm 59.7	<3950	<96000
MR C0037–258.....	221.0 \pm 22.0	248.0 \pm 25.0	286.0 \pm 29.0	518.0 \pm 52.0
6C* 0058+495.....	82.0 \pm 8.3	86.7 \pm 8.8	93.2 \pm 9.5	309.0 \pm 31.0	...	1450.0 \pm 87.3	18900 \pm 1962	<94600
MRC 0114–211.....	87.3 \pm 8.9	117.0 \pm 12.0	157.0 \pm 16.0	398.0 \pm 40.0
TN J0121+1320.....	10.5 \pm 1.8	14.4 \pm 2.1	<32.5	<40.3	<136.0
6C* 0132+330.....	31.6 \pm 3.6	41.3 \pm 4.5	51.9 \pm 12.4	109.0 \pm 11.0
6C 0140+326.....	<623.0	<450.0	34.9 \pm 2.7	36.3 \pm 3.4	194.0 \pm 40.0	2190.0 \pm 110.5	<2580	<20700
MRC 0152–209.....	108.0 \pm 11.0	165.0 \pm 17.0	215.0 \pm 22.0	415.0 \pm 42.0
MRC 0156–252.....	291.0 \pm 29.0	405.0 \pm 41.0	717.0 \pm 72.0	1125.0 \pm 113.0	1430.0 \pm 116.6
TN J0205+2242.....	7.5 \pm 1.7	4.7 \pm 2.3	<29.3	<37.4	<122.0
MRC 0211–256.....	166.0 \pm 17.0	197.0 \pm 20.0	222.0 \pm 22.0	278.0 \pm 28.0	330.0 \pm 42.6
3C 65.....	161.0 \pm 32.0	...	320.0 \pm 66.0
MRC 0251–273.....	11.5 \pm 1.6	12.7 \pm 1.8	<29.1	<28.8	97.2 \pm 34.2
MRC 0316–257.....	19.3 \pm 2.1	20.1 \pm 2.1	19.5 \pm 2.4	38.1 \pm 4.1	<91.5
MRC 0324–228.....	39.4 \pm 4.2	39.7 \pm 4.3	61.1 \pm 8.6	89.9 \pm 9.9
MRC 0350–279.....	23.6 \pm 2.6	40.6 \pm 4.2	82.2 \pm 27.6	79.3 \pm 26.5	...	321.0 \pm 60.7	<1040	<88800
MRC 0406–244.....	40.4 \pm 4.3	43.3 \pm 4.6	<51.6	63.5 \pm 14.5	242.0 \pm 34.6	1420.0 \pm 83.7	24700 \pm 2306	<47700
4C 60.07.....	27.3 \pm 3.1	33.6 \pm 3.7	35.1 \pm 8.4	37.2 \pm 9.5	175.0 \pm 33.0	1340.0 \pm 83.7	<3750	<64600
PKS 0529–549.....	46.6 \pm 4.9	52.9 \pm 5.5	62.7 \pm 8.6	72.2 \pm 9.1	134.0 \pm 33.7	942.0 \pm 71.0	<4110	<74100
WN J0617+5012.....	3.6 \pm 1.0	5.5 \pm 1.2	<48.3	<54.5	<93.4
4C 41.17.....	23.4 \pm 2.4	27.5 \pm 2.8	35.6 \pm 3.7	36.5 \pm 3.5	<99.3	370.0 \pm 43.3	<3210	<26300
WN J0747+3654.....	19.1 \pm 2.4	25.3 \pm 3.0	<29.9	44.9 \pm 11.5	<111.0
6CE 0820+3642.....	79.2 \pm 8.1	81.9 \pm 8.4	82.0 \pm 8.4	68.0 \pm 7.0
USS 0828+193.....	61.7 \pm 6.9	133.0 \pm 13.0	201.0 \pm 21.0	687.0 \pm 74.0	1270.0 \pm 112.8
5C 7.269.....	41.0 \pm 4.5	49.5 \pm 5.3	57.8 \pm 6.1	<40.1	<186.0
6CE 0901+3551.....	37.2 \pm 4.1	46.5 \pm 5.0	52.8 \pm 10.7	69.8 \pm 12.4
6CE 0905+3955.....	51.8 \pm 5.4	60.1 \pm 6.2	96.8 \pm 9.8	146.0 \pm 14.0
B2 0902+34.....	6.4 \pm 0.8	9.9 \pm 1.1	11.0 \pm 2.5	41.3 \pm 2.3	144.0 \pm 39.6	323.0 \pm 18.8	...	<18500
TN J0924–2201.....	11.3 \pm 1.8	11.4 \pm 1.9	<30.6	<33.0	<108.0	<160.0	<3330	<52900
6C 0930+389.....	30.7 \pm 3.4	32.2 \pm 3.6	37.3 \pm 9.2	<32.6	<97.2
USS 0943–242.....	21.5 \pm 2.6	28.4 \pm 3.2	<30.9	25.8 \pm 11.7	109.0 \pm 34.1	493.0 \pm 57.5	<3390	<50900
3C 239.....	96.4 \pm 9.8	111.0 \pm 11.0	130.0 \pm 12.0	142.0 \pm 14.0
MRC 1017–220.....	119.0 \pm 12.0	179.0 \pm 18.0	273.0 \pm 27.0	360.0 \pm 36.0
MG 1019+0534.....	25.6 \pm 2.9	19.5 \pm 3.8	<35.4	<42.9	161.0 \pm 52.5
WN J1115+5016.....	7.8 \pm 2.1	9.5 \pm 3.0	<54.8	<61.1	<88.0
3C 257.....	85.0 \pm 8.7	111.0 \pm 11.0	194.0 \pm 19.0	322.0 \pm 33.0	569.0 \pm 74.6
WN J1123+3141.....	48.2 \pm 5.0	74.4 \pm 7.6	92.7 \pm 9.4	182.6 \pm 18.4	742.0 \pm 70.4
PKS 1138–262.....	318.0 \pm 32.0	497.0 \pm 50.0	887.0 \pm 89.0	1500.0 \pm 150.0	2000.0 \pm 160.3	3890.0 \pm 176.2
3C 266.....	67.9 \pm 7.0	73.1 \pm 7.5	45.1 \pm 4.7	102.6 \pm 10.4
6C 1232+39.....	33.3 \pm 3.6	41.8 \pm 4.4	52.0 \pm 9.2	75.2 \pm 10.8	208.0 \pm 35.9
USS 1243+036.....	22.0 \pm 2.5	21.5 \pm 3.0	<48.0	<62.9	<163.0
TN J1338–1942.....	17.8 \pm 1.9	10.7 \pm 1.2	14.3 \pm 2.8	9.9 \pm 3.4	<119.0
4C 24.28.....	16.5 \pm 2.2	27.3 \pm 3.1	43.3 \pm 8.3	102.0 \pm 10.0	446.0 \pm 50.8
3C 294.0.....	<93.0	<103.0	68.0 \pm 16.8	66.6 \pm 20.6
USS 1410–001.....	50.6 \pm 5.3	79.0 \pm 8.1	166.0 \pm 17.0	240.0 \pm 24.0	481.0 \pm 58.6
8C 1435+635.....	18.6 \pm 2.1	14.7 \pm 2.9	<45.5	<50.3	<86.7	<165.0	<4130	<33900
USS 1558–003.....	78.8 \pm 8.1	101.0 \pm 10.3	105.0 \pm 10.5	233.0 \pm 23.4	398.0 \pm 52.2
USS 1707+105.....	22.1 \pm 2.7	30.1 \pm 3.4	22.6 \pm 9.1	<33.3	<123.0
LBDS 53w002.....	32.0 \pm 3.3	44.0 \pm 4.5	49.9 \pm 5.2	103.0 \pm 11.0	177.0 \pm 33.9	648.0 \pm 61.4	<4300	<65100
LBDS 53w091.....	43.3 \pm 6.3	51.4 \pm 5.3	23.9 \pm 6.1	26.6 \pm 6.4	...	<45.9	<1610	<23900
3C 356.0.....	108.0 \pm 11.0	110.0 \pm 11.0	122.0 \pm 14.0	434.0 \pm 47.0	...	4060.0 \pm 192.3	<4400	<70200
7C 1751+6809.....	46.6 \pm 4.9	50.8 \pm 5.3	<40.9	36.5 \pm 16.0	...	351.0 \pm 50.5	<3600	<51600
7C 1756+6520.....	39.6 \pm 4.2	46.9 \pm 5.0	34.7 \pm 7.7	42.6 \pm 8.6	...	444.0 \pm 51.1	<5900	<151000
3C 368.0.....	126.0 \pm 13.0	112.0 \pm 11.0	112.0 \pm 11.0	210.0 \pm 21.0	...	3250.0 \pm 166.7	28800 \pm 2710	<39000
7C 1805+6332.....	28.4 \pm 3.6	42.1 \pm 4.4	51.4 \pm 5.4	95.6 \pm 17.1	...	648.0 \pm 56.2	<4330	<111000
4C 40.36.....	36.5 \pm 3.9	41.3 \pm 4.3	45.4 \pm 12.9	26.3 \pm 10.3	115.0 \pm 29.4	520.0 \pm 55.2	<4750	<64500
TX J1908+7220.....	200.0 \pm 20.0	229.0 \pm 23.0	241.0 \pm 25.0	480.0 \pm 48.0	841.0 \pm 70.6	1910.0 \pm 98.9	16200 \pm 1905	<63300
WN J1911+6342.....	9.5 \pm 1.8	8.7 \pm 1.8	<26.4	<26.0	<75.3	<142.0	<3710	<57100
TN J2007–1316.....	56.2 \pm 5.9	54.4 \pm 5.8	41.1 \pm 10.7	121.3 \pm 12.3	244.0 \pm 53.5
MRC 2025–218.....	68.4 \pm 7.1	77.1 \pm 8.0	86.8 \pm 10.9	126.8 \pm 12.9	190.0 \pm 50.2
MRC 2048–272.....	59.5 \pm 6.2	72.6 \pm 7.5	78.3 \pm 10.4	38.4 \pm 13.1	<141.0
MRC 2104–242.....	28.1 \pm 3.3	29.7 \pm 3.5	32.8 \pm 10.0	<36.3	121.0 \pm 47.0
4C 23.56.....	61.1 \pm 6.4	86.2 \pm 8.8	126.9 \pm 12.8	423.7 \pm 42.5	1610.0 \pm 129.8	4390.0 \pm 203.8	30300 \pm 2958	<70500

TABLE 3—*Continued*

H ₂ RG	$f_{3.6\ \mu\text{m}}$	$f_{4.5\ \mu\text{m}}$	$f_{5.8\ \mu\text{m}}$	$f_{8.0\ \mu\text{m}}$	$f_{16\ \mu\text{m}}$	$f_{24\ \mu\text{m}}$	$f_{70\ \mu\text{m}}$	$f_{160\ \mu\text{m}}$
MG 2144+1928	22.1 ± 2.7	18.3 ± 2.4	<25.5	<30.3	<93.9
USS 2202+128.....	60.4 ± 6.3	95.8 ± 9.8	120.1 ± 12.1	106.6 ± 10.8	307.0 ± 43.2
MRC 2224–273	61.6 ± 6.4	86.1 ± 8.8	98.4 ± 10.0	203.9 ± 20.5
B3 J2330+3927.....	99.6 ± 10.1	143.0 ± 14.0	160.0 ± 16.0	474.0 ± 47.0	1040.0 ± 88.0	2210.0 ± 113.2	<4670	<64300
4C 28.58	31.6 ± 3.5	36.0 ± 3.9	<41.7	40.9 ± 4.4	228.0 ± 31.5
3C 470	49.5 ± 10.4	75.2 ± 11.8	70.9 ± 10.4	266.0 ± 30.0	...	2650.0 ± 133.5	<5570	<102000

Figure 4 presents the measured mid-IR colors of the 49 H₂RGs with detections in all four IRAC bands and the nine H₂RGs with two-band IRAC detections on the color-color plots of Lacy et al. (2004) and Stern et al. (2005). As expected, the H₂RG sample tends to fall within the AGN wedges identified in each of these diagrams. The Lacy et al. (2004) region includes nearly the entire H₂RG sample: 51 out of 58 (88%) of H₂RGs plotted match the Lacy et al. (2007) color criteria (which are slightly updated from the criteria of Lacy et al. 2004). The smaller Stern et al. (2005) region misses a few more H₂RGs, with only 41 out of 58 H₂RGs (71%) matching the Stern et al. (2005) color criteria. For both plots, nearly every H₂RG is within $1\ \sigma$ of matching the AGN color criteria.

It should be noted that, while the obscured and unobscured AGNs generally lie within the “AGN wedges” in Figure 4, these two classes of luminous AGN are presumed to have different energetics powering their observed mid-IR, IRAC-band SEDs. Luminous, unobscured AGNs tend to have power-law SEDs due to the central engine across the mid-IR regime (e.g., Richards et al. 2006). This leads to rising spectra through the IRAC passbands and places such sources squarely in the wedges at most redshifts. The caveat is that strong features can cause excursions as they redshift into the passbands; e.g., H α at $z \approx 4$ is in the $3.6\ \mu\text{m}$ band (e.g., C. Bian et al. 2007, in preparation). In contrast to this, we presume that starlight plays a dominant role in the shorter

wavelength IRAC passbands for most obscured AGNs, with AGN-heated dust dominating the reddest IRAC passbands. Indeed, a clear dip between the stellar component and the hot dust component is seen in many sources in our sample. Consider, as an example, the left-hand panel of Figure 3. The redshifted galaxy tracks have $[3.6] - [4.5] > 0.2$ (Vega) at $z \gtrsim 1$ due to the $1.6\ \mu\text{m}$ peak of the stellar SED redshifting into the $4.5\ \mu\text{m}$ IRAC passband. The red $[3.6] - [4.5]$ colors are then usually due to the $z > 1$ stellar populations, while the red $[5.8] - [8.0]$ colors are due to the AGN. The next section will concern using the longer wavelength *Spitzer* data to model and subtract the AGN contribution to the mid-IR SEDs of our sample, and thus to derive the rest-frame near-IR stellar luminosities.

4. MODELING OF THE REST-FRAME NEAR-INFRARED AND MID-INFRARED

We begin our analysis of the broadband IR SEDs by considering the galaxies with the most extensive *Spitzer* coverage. This smaller sample of 26 galaxies illustrates the shape and range of H₂RG SEDs in the IR (§ 4.2) and is then used to inform analysis of the sources with more restricted *Spitzer* imaging (§ 4.3).

Despite the extensive near-IR data available for many of the H₂RGs, we elect not to include these data in the SED fitting (although the *K*-band photometry is overplotted in the SED plots).

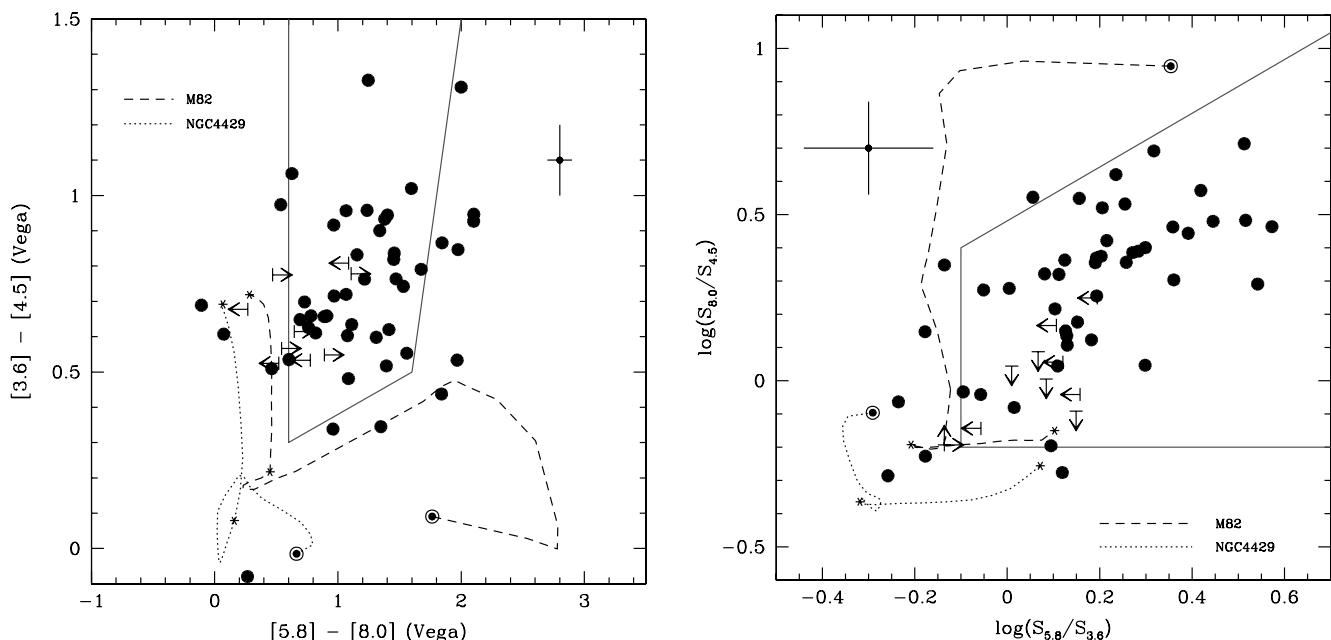


FIG. 4.—Mid-IR colors of H₂RGs. Solid lines indicate empirical criteria that separate (type 1) active galaxies from Galactic stars and normal galaxies. The left panel shows the criteria from Stern et al. (2005); the right panel shows the criteria originally from Lacy et al. (2004), but updated in Lacy et al. (2007). Note that the axes have been selected to facilitate comparison with the original works. Crosses indicate typical uncertainties on the mid-IR photometry. H₂RGs are the quintessential type 2, luminous AGNs. As expected, they generally reside with the empirical AGN wedges. Tracks from redshift 0 to 2 for a late-type starburst galaxy (M82; dashed line) and an early-type galaxy (NGC 4429; dotted line) are included. These template SEDs are from Devriendt et al. (1999); circles mark the $z = 0$ starting points, and asterisks indicate $z = 1$ and $z = 2$ for the tracks. The tracks indicate that neither galaxy would be selected as an AGN candidate if located below $z = 2$. [See the electronic edition of the Supplement for a color version of this figure.]

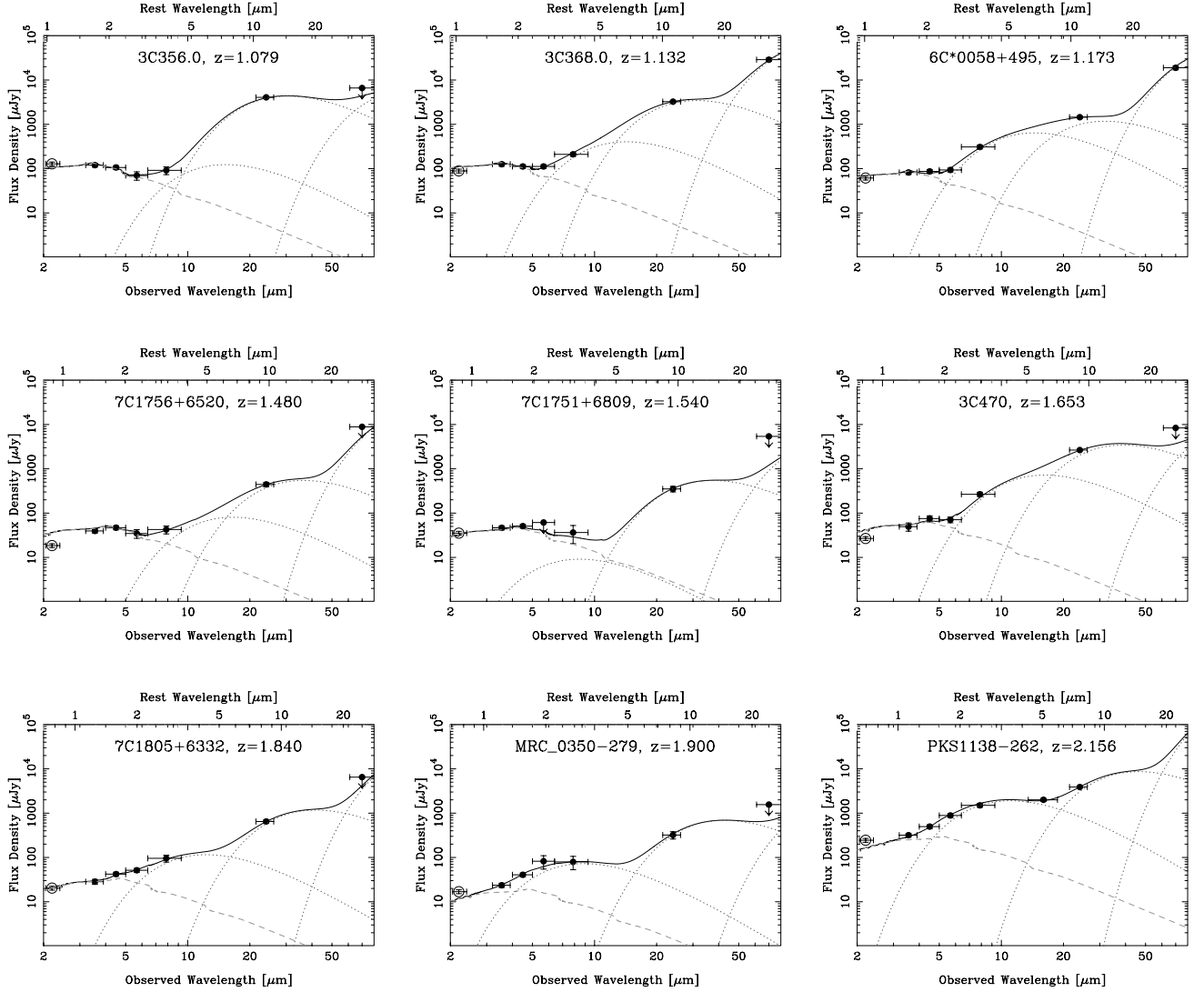


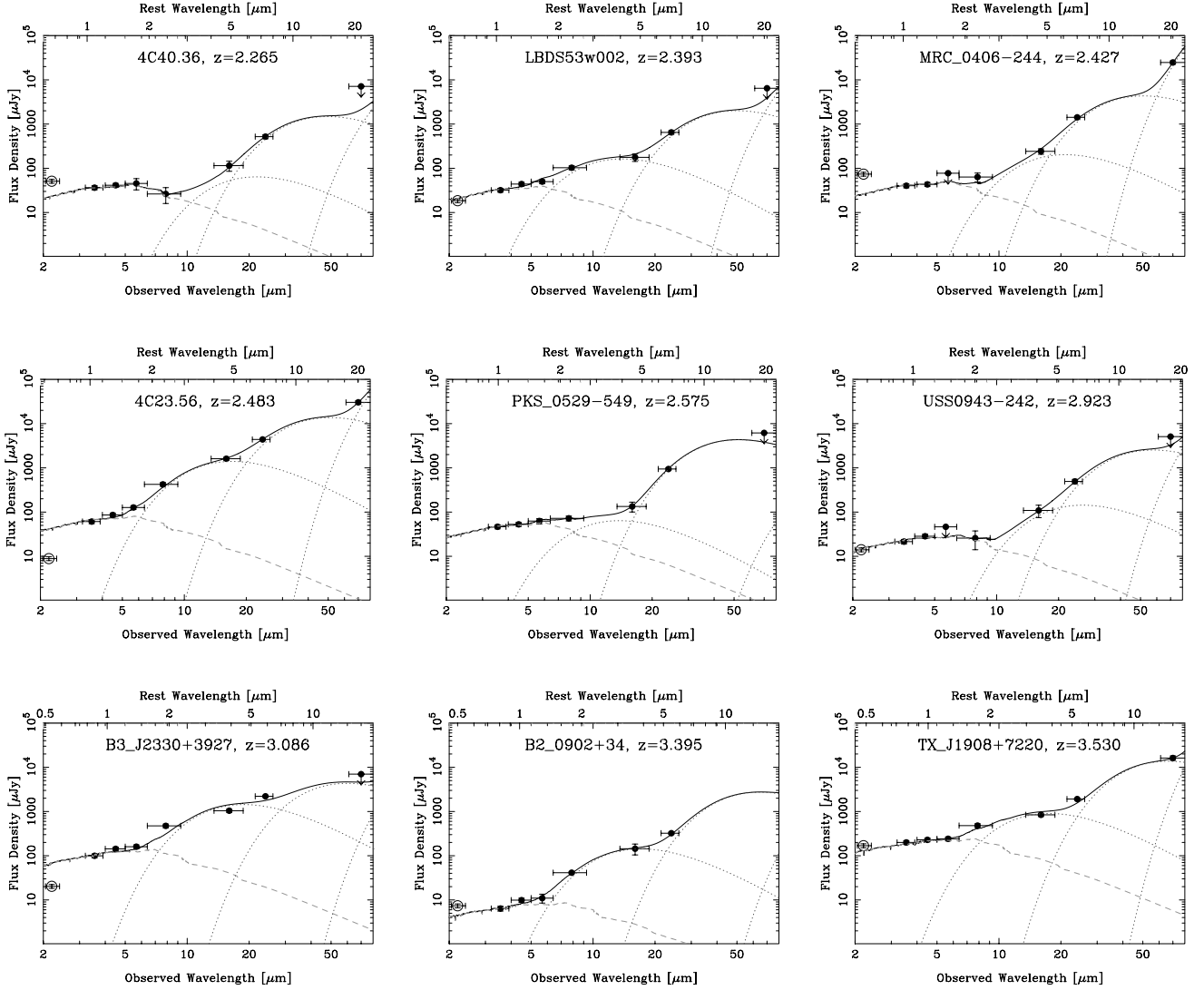
FIG. 5.—SED fitting of 21 sources with both IRAC observations and MIPS detections. The name of each HzRG and its redshift are marked at the top of the panel. Observed wavelength is along the bottom axis and rest-frame wavelength is along the top axis. Data with error bars are presented as filled circles; open circles are not used in the fitting for reasons described in the text. Downward arrows indicate upper limits. The solid dark line indicates the total best-fit SED. The stellar and dust components are indicated by dashed and dotted lines, respectively. [See the electronic edition of the Supplement for a color version of this figure.]

This omission has several reasons and, as described in § 5, should have minimal impact on the derived stellar masses, the primary goal of our analysis. Foremost, we omit the near-IR data as it samples the rest-frame UV to optical wavelengths of our high-redshift galaxies. At these wavelengths, several issues arise. First, the scattered and direct AGN continuum is blue in color and will thus be a larger contributor to the SED at wavelengths below 4000 \AA (e.g., Vernet et al. 2001). Second, high equivalent width emission lines can significantly affect the near-IR photometry for certain redshifts (e.g., Villar-Martín et al. 2006). Indeed, when $H\alpha$ is in the bluest IRAC channels (for our highest redshift sources), we do not include the affected channel in the SED modeling. Third, possible contributions from younger stellar populations will be most pronounced at shorter wavelengths. Fourth, rest-frame optical and UV data are more susceptible to dust extinction than rest-frame near-IR data. The final reason to omit the near-IR data is the large inhomogeneity of the data quality, depth, and analysis techniques. We are generally relying on published photometry done on 3 m to 10 m telescopes over the past two decades and extracted with a range of aperture sizes. Only in a few cases are we able to obtain the images from telescope archives.

For the sake of homogeneity of the analysis, the SED modeling described below relies solely on *Spitzer* photometry. In a forthcoming paper, we study the detailed stellar population properties of the HzRG sample, combining *Spitzer* data with archival data and data from our ongoing observing campaigns at Palomar Observatory and the VLT (A. Rettura et al. 2007, in preparation). For a few galaxies, we have already performed the full analysis using all available (optical to mid-IR) data (e.g., Villar-Martín et al. 2006; Stern et al. 2006; C. De Breuck et al. 2007, in preparation). As shown in § 5, the derived stellar masses are consistent with the results of the simpler analysis presented here.

4.1. The Model

Twenty-six of our radio galaxies have both IRAC and MIPS observations, of which only four are not detected at $24 \mu\text{m}$ (or in the longer wavelength MIPS channels). These four sources include three of the highest redshift radio galaxies and one radio galaxy at $z \sim 1.5$. In the latter case, this nondetection may be indicative of silicon absorption at rest-frame $9.8 \mu\text{m}$. Alternatively, the undetected $z \sim 1.5$ radio galaxy, LBDS 53W091, is a low-luminosity radio source, and Stern et al. (2006) argue that its

FIG. 5—*Continued*

mid-IR nondetection likely indicates a SED dominated by old stellar populations and not by hot, AGN-heated dust. One source, 6C 0140+326, cannot be distinguished from a bright foreground galaxy at 3.6 and 4.5 μm , so we do not use it in our modeling here. Hence, our final sample numbers 21 HzRGs with IRAC and MIPS detections.

For the 21 HzRGs with MIPS detections, we fit the SEDs with toy models comprised of a composite stellar population (CSP) and multiple blackbody (BB) dust components. Our primary goal is to simply derive the rest-frame near-IR stellar luminosity, which can then be translated into a stellar mass assuming reasonable stellar population synthesis models (§ 5). We are also, in these cases with MIPS detections, able to estimate the rest-frame 5 μm monochromatic luminosities, a possible measure of the obscured AGN power (Ogle et al. 2006). The difficulty is that in many sources a steeply rising continuum is visible in the redder IRAC bands, indicative of the tail of hot, AGN-heated dust contaminating the rest-frame near-IR emission. Owing to the sparse sampling of the SEDs at these wavelengths, our goal is not to fully explore the astrophysics of the continuum emission at these wavelengths, but to use the MIPS (and IRS, where available) photometry to model the dust SED and subtract its contribution at rest-frame near-IR wavelengths. We do not apply Galactic extinction cor-

rections as they are negligible ($<0.5\%$) at the *Spitzer* wavelengths. Also, since emission lines longward of $H\alpha$ are not strong enough to significantly affect our modeling (e.g., Haas et al. 2005; Ogle et al. 2006; Cleary et al. 2007), they are ignored in the analysis. Additional systematic issues in our modeling are discussed in §§ 4.4 and 6.3, but we stress here that the stellar masses are very insensitive to the choice of BBs for the longer wavelength component.

We model the radio galaxy IR SEDs with a four-component model consisting of an elliptical galaxy CSP template and three BBs of different dust temperatures. Best-fit parameters for the models are determined using standard χ^2 minimization techniques. The uncertainties on the flux densities used to determine the χ^2 of a specific fit include both random (from the observations) and systematic (e.g., the detector zero points and the shape of the SED) uncertainties, which are added in quadrature (see § 3). The full fitting is only done for sources with MIPS 24 μm detections as we need both enough data points to fit our model and a detection longward of the IRAC bands to provide sufficient leverage on the dust component (see § 4.2). For sources without MIPS detections or observations we do not have enough data points to perform a secure fit of this four-component model. Hence, in many cases we only get an upper limit to the stellar component, although

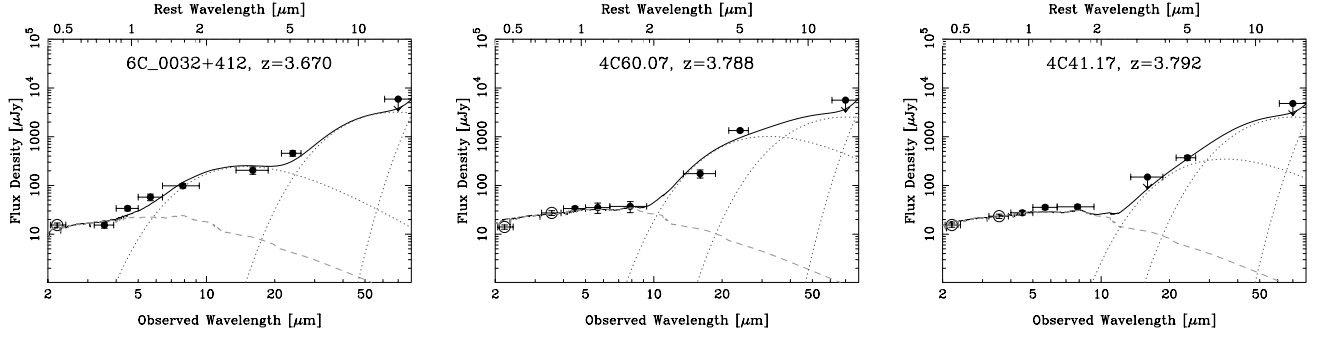


FIG. 5—Continued

in some cases we can get a likely value for the stellar luminosity when the IRAC bands fit the stellar component well (see § 4.3).

4.1.1. Stellar Component

The CSP template used in our SED modeling consists of an elliptical galaxy modeled with PÉGASE.2 (Fioc & Rocca-Volmerange 1997). The adopted star formation history (SFH) scenario has been shown to result in reliable photometric redshifts with the code Z-PEG (Le Borgne & Rocca-Volmerange 2002) and to well reproduce early-type galaxy SEDs (from rest-frame UV to near-IR) up to $z \sim 1.25$ (Rettura et al. 2006). Specifically, the star-formation rate is proportional to the gas density, $\text{SFR} \propto \rho_{\text{gas}}$, and the astration (recycling) rate is equal to 3.33 Gyr^{-1} . Gaseous exchanges with the interstellar medium are represented by infall and galactic winds. The former process simulates mass growth, and the latter represses any star-formation after the first Gyr by dissipating the gas from the galaxy and hence driving the gas fraction toward zero. The reader is referred to the aforementioned papers for more details on the adopted template parameters and the star-formation histories. In addition, Rocca-Volmerange et al. (2004) demonstrates how this elliptical galaxy model works for the most massive galaxies that populate the lower envelope of the K - z relation. For the current work, we use a Kroupa (2001) initial mass function (IMF) and dust-free model templates. We note that in

the templates used here, the metallicity is not a free parameter; it evolves consistently with the SFH, reaching solar values at the ages of interest in this study. We assume a galaxy formation redshift of $z_{\text{form}} = 10$, and we discuss the systematic effects of this choice, along with the other details of the galaxy models in § 6.3. In brief, however, although the derived stellar masses vary somewhat with the model choices (mainly by a simple offset depending on the choice of IMF), we find that the derived luminosities are relatively robust against model uncertainties for stellar population ages greater than 1 Gyr.

4.1.2. Dust Component

The longer wavelength modeling assumes three dust components, each of a different temperature. The coldest of the BBs is chosen to have a temperature 60 K, representative of the large cool dust reservoirs associated with radio galaxies (e.g., Greve et al. 2006), although this component does not contribute to the rest-frame near-IR. The second BB component has a fixed temperature of 250 K. For the final, hotter BB component we allowed the temperature to vary from 500 to 1500 K (in steps of 50 K) and interpret it as being associated with hot dust heated by the central AGN. This upper limit of 1500 K was chosen as dust sublimates at this temperature. Systematic effects from the chosen BB temperatures are discussed in § 6.3; in brief, we find they have little

TABLE 4
RESULTS OF SED FITTING FOR HzRGs WITH MIPS DETECTIONS

HzRG	$\log(L_{\text{H}}^{\text{tot}}/L_{\odot})$	$\log(L_{\text{H}}^{\text{stel}}/L_{\odot})$	f_{stel}	$\log(M^{\text{stel}}/M_{\odot})$	$\log(L_{5\text{ }\mu\text{m}}/L_{\odot})$
6C 0032+412	12.13	$11.47^{+0.16}_{-0.12}$	0.22	$11.28^{+0.16}_{-0.12}$	$11.97^{+0.56}_{-0.24}$
6C* 0058+495	11.16	$11.16^{+0.13}_{-0.10}$	0.99	$11.26^{+0.13}_{-0.10}$	$11.40^{+0.16}_{-0.11}$
MRC 0350–279	11.29	$10.80^{+0.26}_{-0.17}$	0.40	$10.85^{+0.26}_{-0.17}$	$10.91^{+0.50}_{-0.23}$
MRC 0406–244	11.50	$11.49^{+0.13}_{-0.13}$	0.98	$11.38^{+0.13}_{-0.13}$	$11.75^{+0.11}_{-0.10}$
4C 60.07	11.67	$11.65^{+0.13}_{-0.10}$	0.95	$11.44^{+0.13}_{-0.10}$	$12.50^{+0.35}_{-0.35}$
PKS 0529–549	11.67	$11.60^{+0.11}_{-0.10}$	0.86	$11.46^{+0.11}_{-0.10}$	$11.60^{+0.14}_{-0.10}$
4C 41.17	11.60	$11.60^{+0.08}_{-0.08}$	0.99	$11.39^{+0.08}_{-0.08}$	$12.06^{+0.36}_{-0.36}$
B2 0902+34	11.52	$10.97^{+0.14}_{-0.11}$	0.28	$10.81^{+0.14}_{-0.11}$	$11.80^{+0.17}_{-0.12}$
USS 0943–242	11.40	$11.40^{+0.15}_{-0.07}$	0.99	$11.22^{+0.15}_{-0.07}$	$11.67^{+0.35}_{-0.20}$
PKS 1138–262	12.59	<12.18	<0.39	<12.11	$12.39^{+0.35}_{-0.20}$
LBDS 53w002	11.55	$11.38^{+0.12}_{-0.10}$	0.68	$11.27^{+0.12}_{-0.10}$	$11.55^{+0.22}_{-0.14}$
3C 356.0	11.28	$11.28^{+0.12}_{-0.10}$	1.00	$11.39^{+0.12}_{-0.10}$	$11.39^{+0.08}_{-0.07}$
7C 1751+6809	11.14	$11.12^{+0.13}_{-0.13}$	0.95	$11.14^{+0.13}_{-0.13}$	$10.39^{+0.30}_{-0.18}$
7C 1756+6520	11.12	$11.12^{+0.12}_{-0.10}$	1.00	$11.15^{+0.12}_{-0.10}$	$10.80^{+0.27}_{-0.17}$
3C 368.0	11.32	$11.32^{+0.11}_{-0.09}$	0.99	$11.43^{+0.11}_{-0.09}$	$11.28^{+0.10}_{-0.08}$
7C 1805+6332	11.22	$11.11^{+0.15}_{-0.11}$	0.78	$11.07^{+0.15}_{-0.11}$	$11.19^{+0.17}_{-0.13}$
4C 40.36	11.38	$11.38^{+0.13}_{-0.10}$	1.00	$11.29^{+0.13}_{-0.10}$	$11.21^{+0.23}_{-0.15}$
TX J1908+7220	12.63	<12.44	<0.64	<12.27	$12.60^{+0.13}_{-0.11}$
4C 23.56	11.91	$11.71^{+0.12}_{-0.09}$	0.63	$11.59^{+0.12}_{-0.09}$	$12.49^{+0.10}_{-0.09}$
B3 J2330+3927	12.30	<12.11	<0.64	<11.94	$12.58^{+0.26}_{-0.16}$
3C 470	11.32	$11.30^{+0.21}_{-0.15}$	0.95	$11.30^{+0.21}_{-0.15}$	$11.80^{+0.11}_{-0.09}$

effect on the derived stellar masses. We have also experimented with toroidal AGN models (e.g., Pier & Krolik 1992; Granato et al. 1997; Nenkova et al. 2002; Siebenmorgen et al. 2004). However, the paucity of our infrared data, consisting simply of photometric points and not infrared spectra, makes fitting with detailed models ill-constrained. We emphasize that this dust modeling is not completely physical; however, the modeling is sufficient for the primary goal of this paper, which is to simply estimate and subtract any contribution by (hot) dust to the rest-frame near-IR emission.

4.2. Fits to HzRGs with MIPS Detections

The best-fit models for the 21 HzRGs with MIPS detections are shown in Figure 5. Observed wavelength is indicated along the bottom axis, and rest wavelength is on the top axis. Open circles, not used in the fitting, are either (1) *K*-band data or (2) potentially contaminated by strong emission lines (e.g., $H\alpha$). Upper limits are indicated by downward arrows. We separate the contribution of host dust and stellar emission at rest-frame *H* band, which can then be used to derive stellar masses (§ 5). Table 4 presents the total *H*-band luminosities, the stellar *H*-band luminosities, the stellar fractions at *H* band, stellar masses, and rest-frame $5\ \mu\text{m}$ monochromatic luminosities for sources with full SED fitting. This fiducial mid-IR wavelength, $5\ \mu\text{m}$, was selected as it is always shortward of the $24\ \mu\text{m}$ MIPS observations, even for our most distant HzRGs with $24\ \mu\text{m}$ detections ($z \sim 3.8$). The formal χ^2 uncertainties (95.4% confidence limits) of the stellar luminosities from the fitting are listed in Table 4. They are generally of the order $\sim 25\%$ and are mainly due to the uncertainty in the IRAC flux densities, which, in turn, are dominated by systematics.

4.3. Fits to HzRGs without MIPS Observations or Detections

We can constrain, or in some cases quantify, the stellar luminosities for sources without MIPS observations or detections using the results of the full SED fitting described above (see Table 5). For many HzRGs we clearly observe the *H*-band stellar peak (see Fig. 5). Even in those cases where we do not see the *H*-band peak, IRAC channels 1 and 2 are typically dominated by the stellar component. At the least, we can obtain an upper limit to the stellar mass by demanding that the stellar component does not exceed any of the IRAC photometric points. Hence, we can obtain upper limits to the stellar masses of these HzRGs. Typically, this upper limit is restricted by just IRAC channel 1, as the observed mid-IR SEDs are often quite red. In many cases, the maximum fit is constrained by IRAC channels 1 and 2, and occasionally by longer wavelength channels. In almost half of the radio galaxy sample, the stellar SED is well fitted in two or three channels (those at shorter wavelength), so we nominally fit the SED and derive stellar luminosities. The results of the fitting for the HzRGs without MIPS observations or detections are shown in Figure 6, which adopts the same symbol convention as Figure 5 bar the inclusion of BB dust components. As can be seen, the $16\ \mu\text{m}$ observations, where present, generally show a strong excess above the maximally fitted stellar template. In what follows, we distinguish those HzRGs whose IRAC SEDs are well fitted by a stellar population (e.g., where multiple IRAC channels are well fitted by the stellar SED model) from those where the IRAC photometry has merely provided an upper limit to the rest-frame near-IR stellar luminosity.

4.4. Systematic Effects in the SED Modeling

We discuss here two possible systematic effects in the SED modeling: the adopted BB temperatures and potential photometric offsets in the longer wavelength photometry due to strong

TABLE 5
RESULTS OF SED FITTING FOR HzRGs WITH NO MIPS DETECTIONS

HzRG	$\log(L_{\text{H}}^{\text{tot}}/L_{\odot})$	$\log(M_{\text{max}}^{\text{stel}}/M_{\odot})$	$\log(L_{5\ \mu\text{m}}/L_{\odot})$
MRC 0037–258	<11.56	<11.70	...
MRC 0114–211	<11.37	<11.40	...
TN J0121+1320	11.21	11.00	...
6C* 0132+330	11.11	11.10	...
6C 0140+326	<11.78	<11.40	...
MRC 0152–209	<11.72	<11.70	...
MRC 0156–252	<12.23	<12.20	12.21
TN J0205+2242	<10.96	<10.80	...
MRC 0211–256	<11.54	<11.60	11.23
3C 65	11.44	11.50	...
MRC 0251–273	11.14	11.00	...
MRC 0316–257	11.39	11.20	...
MRC 0324–228	11.21	11.20	...
WN J0617+5012	10.74	10.60	...
WN J0747+3654	11.34	11.20	...
6CE 0820+3642	11.54	11.50	...
USS 0828+193	<11.72	<11.60	12.34
5C 7.269	11.48	11.40	...
6CE 0901+3551	11.32	11.30	...
6CE 0905+3955	11.40	11.40	...
TN J0924–2201	11.48	11.10	<11.79
6C 0930+389	11.40	11.30	...
3C 239	11.60	11.60	...
MRC 1017–220	<11.74	<11.70	...
MG 1019+0534	<11.34	<11.20	11.50
WN J1115+5016	<10.86	<10.70	...
3C 257	<11.83	<11.70	11.96
WN J1123+3141	<11.81	<11.60	...
3C 266	11.22	11.30	...
6C 1232+39	<11.66	<11.50	...
USS 1243+036	<11.47	<11.30	...
TN J1338–1942	<11.26	<11.00	...
4C 24.28	<11.20	<11.00	...
3C 294.0	<11.50	<11.50	...
USS 1410–001	<11.53	<11.40	11.86
8C 1435+635	<11.45	<11.10	<11.63
USS 1558–003	11.85	11.70	11.83
USS 1707+105	11.28	11.20	...
LBDS 53w091	11.20	11.20	<10.88
WN J1911+6342	<11.13	<10.90	<11.33
TN J2007–1316	<11.79	<11.60	...
MRC 2025–218	11.80	11.60	11.53
MRC 2048–272	<11.55	<11.50	...
MRC 2104–242	11.34	11.20	11.30
MG 2144+1928	<11.48	<11.30	...
USS 2202+128	<11.85	<11.70	11.77
MRC 2224–273	<11.34	<11.30	...
4C 28.58	<11.56	<11.40	11.68

spectral features redshifting into the *Spitzer* passbands. The latter effect mimics the effects of alternate SEDs with strong absorption and/or emission features. As seen below, neither systematic issue strongly affects the derived rest-frame near- and mid-IR luminosities.

As the cooler dust components have negligible influence at rest-frame *H* band, the exact temperatures used are not vital to the final derived stellar luminosities and masses. Modeling observations of 3C radio galaxies obtained with the *Infrared Space Observatory*, Rocca-Volmerange & Remazeilles (2005) find the far-IR SEDs are well fitted with two BB components of temperatures 40 ± 16 and 340 ± 50 K. Archibald et al. (2001) modeling submillimeter observations of HzRGs, likewise adopts an optically thin, isothermal gray-body of temperature 40 K. When

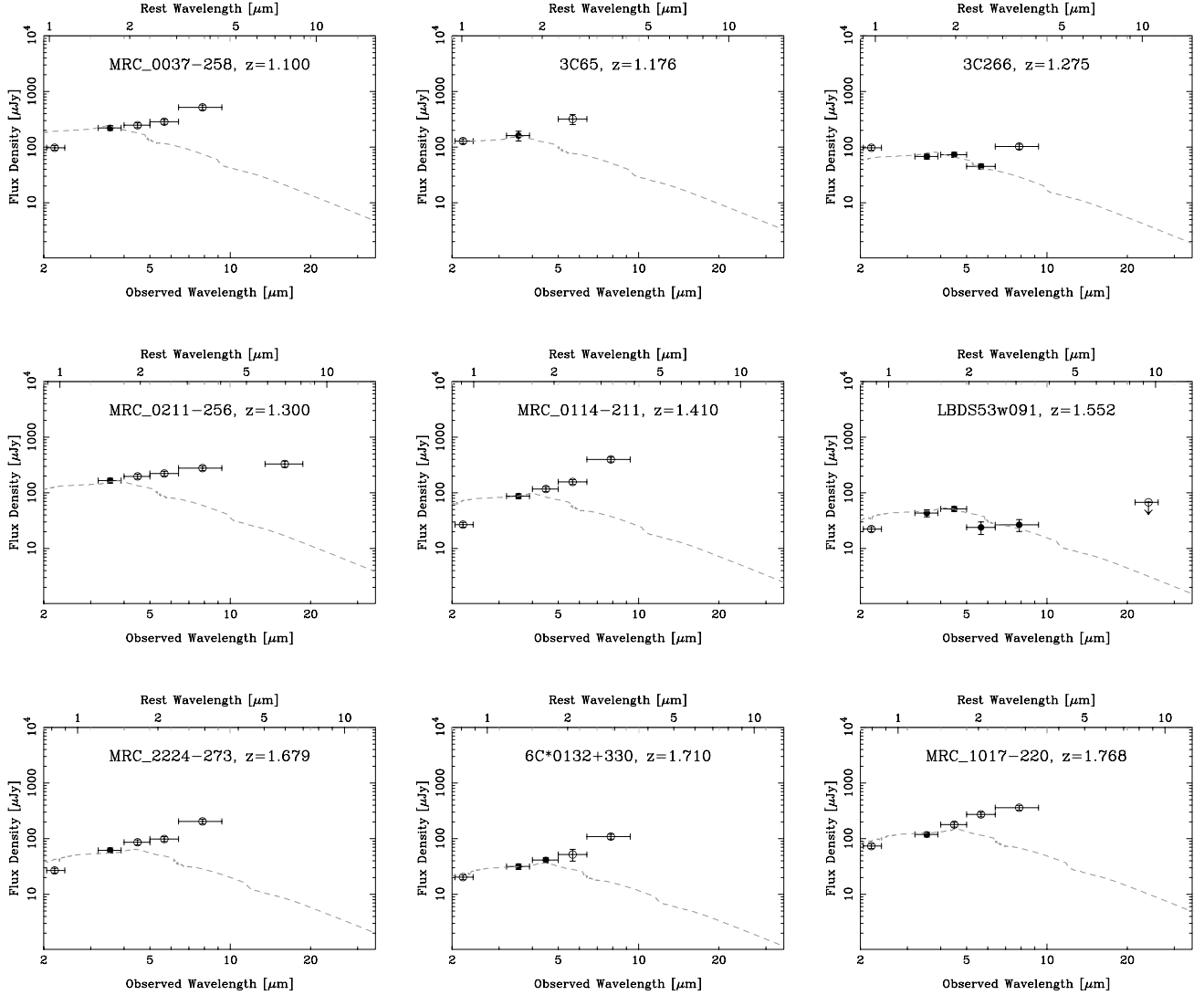


FIG. 6.— Galaxy SED fits to determine stellar masses or upper limits. The name of each HzRG and its redshift are marked at the top of the panel. Observed wavelength is along the bottom axis and rest-frame wavelength is along the top axis. Data with error bars are presented as filled circles; open circles not used in the fitting are described in the text. Downward arrows indicate upper limits. The dashed line indicates the total best-fit SED. [See the electronic edition of the Supplement for a color version of this figure.]

we redo our analysis adopting this cooler cold dust component rather than the previously adopted 60 K, the derived rest-frame near/mid-IR luminosities change by less than 0.1%. Likewise, using the 340 K warm dust component of Rocca-Volmerange & Remazeilles (2005) instead of the previously adopted 250 K, we find that the derived rest-frame near-IR luminosities change by less than 0.1%, although the mid-IR luminosities increase by $\sim 40\%$.

The fitting algorithm we adopt assumes a very simplistic model of the long-wavelength HzRG SED. No HzRGs have been observed to have PAH features (Ogle et al. 2006; Cleary et al. 2007), but some less luminous, radio-quiet type 2 AGNs have been seen with PAH features (M. Lacy et al. 2007, in preparation). Silicon absorption has been observed in HzRGs (Ogle et al. 2006), but even with a line width of $1.4 \mu\text{m}$ and $\tau = 1.5$ we would only observe a 30%–40% decrease in the observed flux density. Ogle et al. (2006) also note that there are indications that the power-law continuum is truncated at the sublimation temperature.

We have investigated the effects of these potential features by rerunning the fitting procedure, varying the 16 and $24 \mu\text{m}$ flux densities to simulate those passbands falling on strong emission or absorption features. We varied the $16 \mu\text{m}$ flux densities by

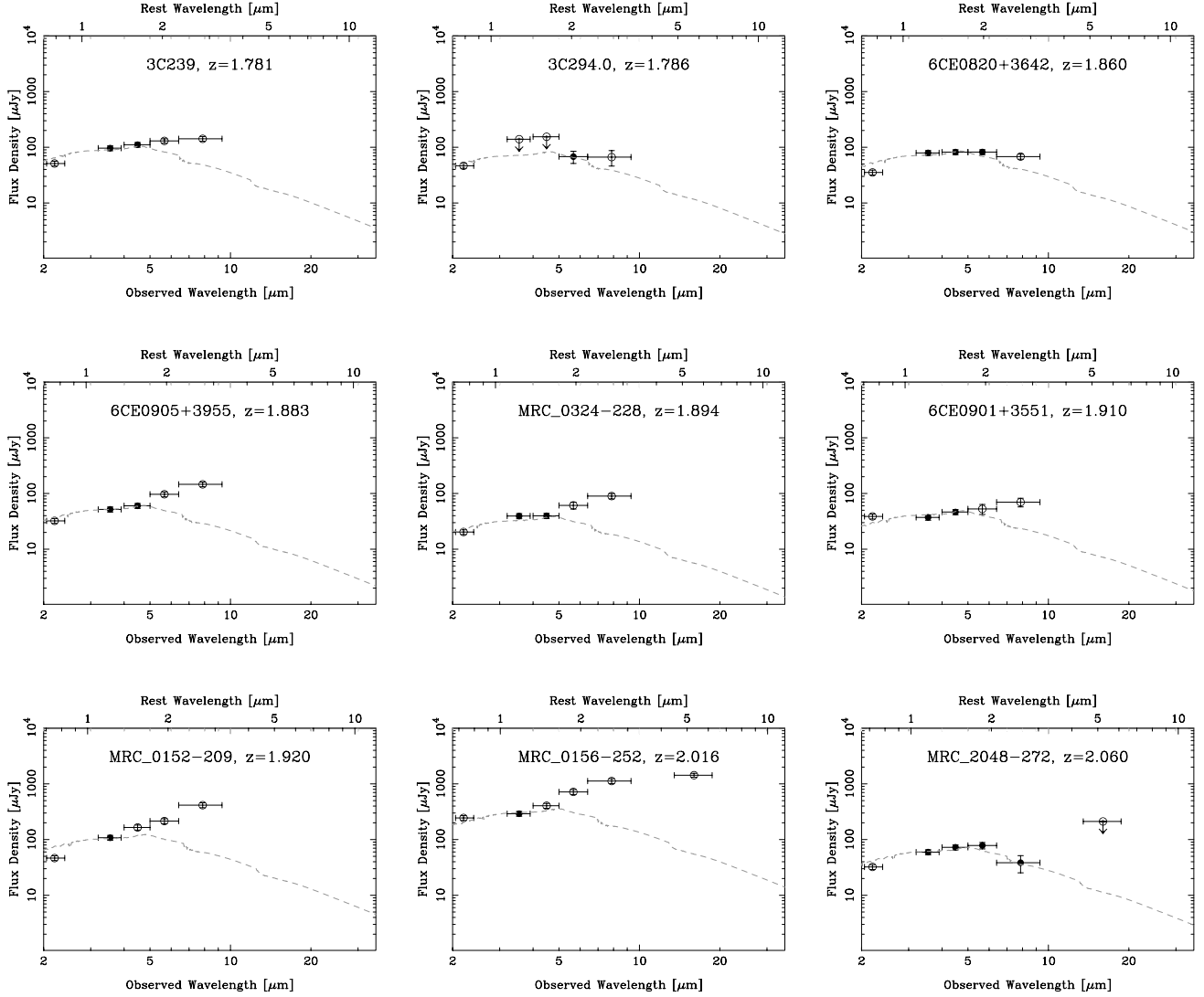
10% to account for weaker PAH features at $6.4 \mu\text{m}$ passing through the IRS bandpass. We varied the $24 \mu\text{m}$ flux densities by 50% to account for both the strong $7.7 \mu\text{m}$ PAH emission feature and the strong $9.8 \mu\text{m}$ silicate absorption feature. These experiments only changed the mean $5 \mu\text{m}$ luminosities by $\sim 5\%$ (for varying the $16 \mu\text{m}$ flux density) and $\sim 25\%$ (for varying the $24 \mu\text{m}$ flux density). Given the lack of observational evidence for these features so far we consider these estimates conservative. The effects on the mean stellar luminosity (and hence mass) are $\lesssim 2\%$ in both cases.

5. RESULTS OF SED FITTING

5.1. Stellar Fractions

Figures 7 and 8 show the fraction of the HzRG rest-frame H -band luminosity that is modeled as stellar in origin, plotted against total H -band luminosity, stellar H -band luminosity, redshift, radio power, and rest-frame $5 \mu\text{m}$ luminosity. The stellar fraction is defined as the ratio of the flux densities found from convolving the stellar and total SEDs with a H -band filter curve.

Only the 21 HzRGs with MIPS detections are presented in these figures and their H -band luminosities (stellar and total), stellar

FIG. 6—*Continued*

fractions, inferred stellar masses (see § 6), and monochromatic $5\ \mu\text{m}$ luminosities (see § 5.4) in Table 4. As can be seen, half the sample has the rest-frame near-IR luminosity strongly dominated by starlight, with $\geq 95\%$ of the emission apparently stellar in origin. Another 20% of the sample have stellar emission accounting for 60%–90% of the rest-frame near-IR flux and thus still dominate the emission at this wavelength. There appears to be a weak inverse correlation between stellar fraction and *total* H -band luminosity, while the stellar fraction does not vary with *stellar* H -band luminosity. This suggests that the underlying host galaxy population is homogeneous. No evolutionary trends in the stellar fraction are evident, nor does the stellar fraction appear to correlate with either radio power or rest-frame mid-IR luminosity. This result is expected for the following reasons. The radio emission at rest-frame 3 GHz is dominated by isotropic lobe emission. Likewise, rest-frame mid-IR samples largely isotropic emission coming from near the central engine (e.g., Heckman et al. 1994); at these wavelengths, the emission should be largely immune to extinction. The stellar fraction at H band, however, is very dependent on obscuration of the AGNs, which, in the currently preferred unified schemes (e.g., Antonucci 1993; Urry & Padovani 1995), is a function of orientation. AGNs with little obscuration of the central engine will have higher rest-frame near-IR luminosities, show broad lines, and have low stellar frac-

tions. Indeed, the three sources in our MIPS sample with the highest rest-frame H -band luminosities, PKS 1138–262, TX J1908+7220, and B3 J2330+3927, both show AGN signatures in the near-IR (see Appendix) and are indicated as upper limits in Table 4 and the relevant figures (Figs. 7 and 8). The stellar fraction is expected to be an indicator of orientation and should thus not correlate with the orientation-independent parameters. In a future publication (N. Seymour et al. 2007, in preparation), we shall analyze how the stellar fraction correlates with properties that are expected to depend on orientation, such as radio core fraction and radio spatial extent.

5.2. Rest-Frame Near-IR Stellar Luminosities

The rest-frame H -band stellar luminosities are found mainly to lie in the 10^{11} – $10^{12}\ L_{\odot}$ range, as illustrated in Figure 9. Overlaid are PÉGASE models illustrating the luminosity of an elliptical galaxy model with $z_{\text{form}} = 10$ for masses of 10^{11} and $10^{12}\ M_{\odot}$. The derived HzRG stellar luminosities are consistent with extremely massive hosts, with masses of a few $\times 10^{11}\ M_{\odot}$ out to $z = 4$. Derivations of masses and their associated uncertainties are presented in § 6.

This result confirms earlier work on the masses of radio galaxies. Rocca-Volmerange et al. (2004) find that most radio galaxies have K -band magnitudes consistent with stellar masses

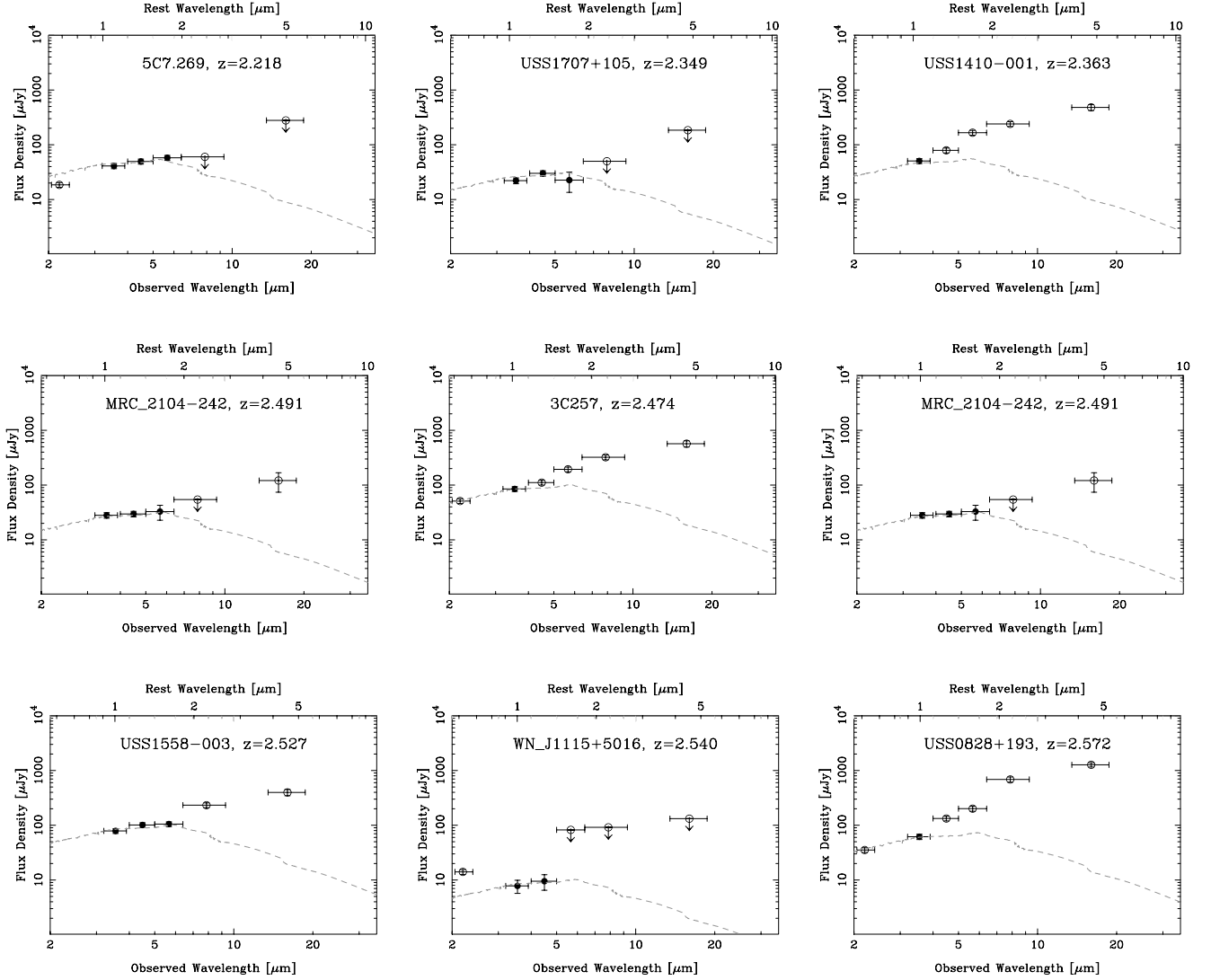


FIG. 6—Continued

of 10^{11} – $10^{12} M_{\odot}$ with a few having magnitudes implying masses $>10^{12} M_{\odot}$. These sources with bright K -band magnitudes may have emission lines or scattered AGN light contributing to them, so their K -band magnitudes should be viewed as upper limits.

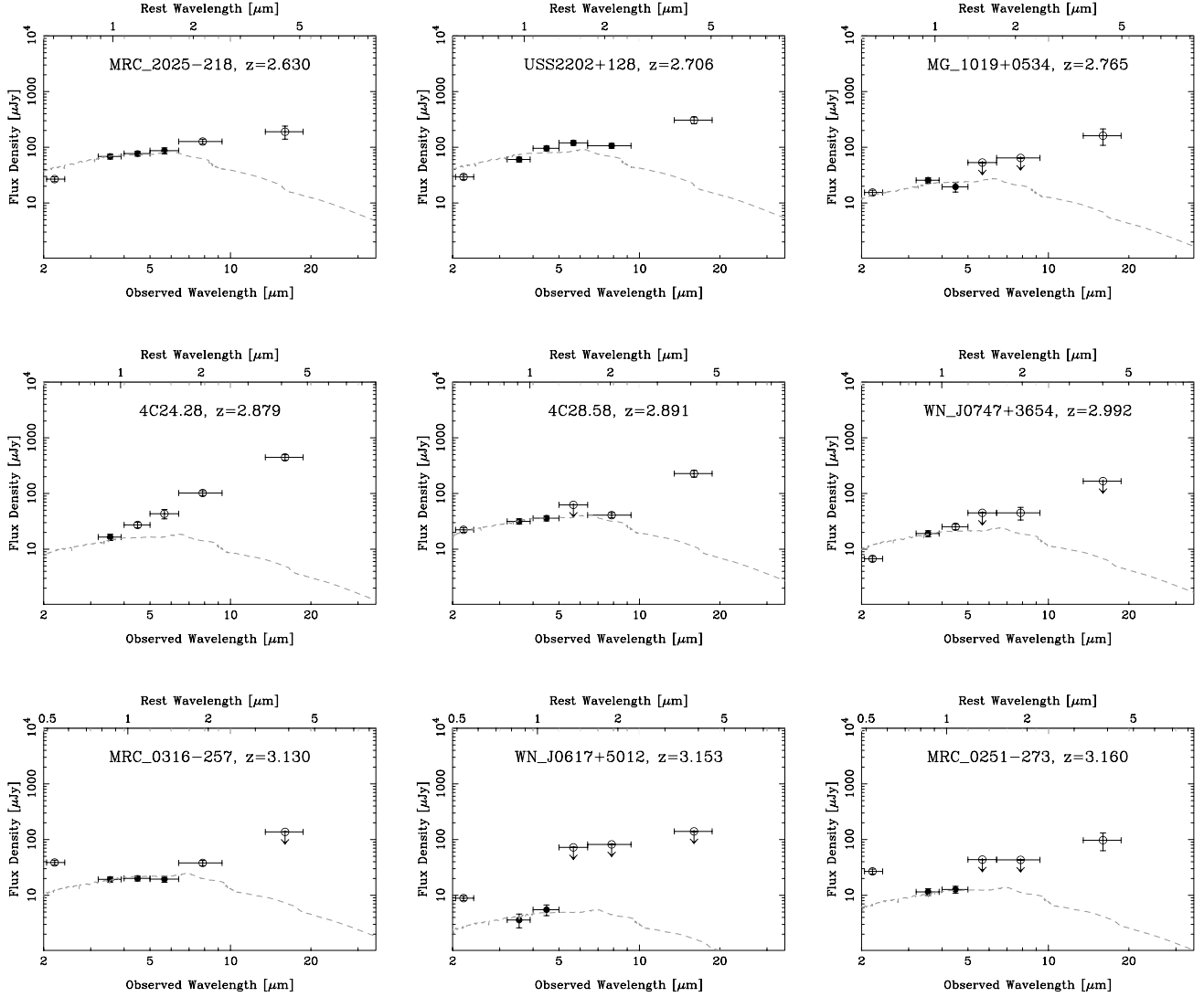
We also plot the rest H -band stellar luminosities of a sample of submillimeter galaxies (SMGs) in the GOODS North region from Borys et al. (2005) as red crosses in Figure 9. The H -band luminosities are rederived using our modeling technique with the data presented in Borys et al. (2005). Our analysis produces similar luminosities to Borys et al. (2005). However, due to different assumed star formation histories and IMFs, our derived stellar masses systematically differ by 25%. These SMGs have a similar range of rest-frame H -band luminosities to the HzRGs, implying similar stellar masses. There is a probable evolutionary link between SMGs and HzRGs, although the number of similarities between these populations is comparable to the number of differences. On the one hand, SMGs have a much higher areal density than HzRGs: the former are relatively numerous in small-area (100 arcmin²) surveys (e.g., Borys et al. 2003), while the latter are much rarer and typically herald from large-area or full-sky radio surveys. On the other hand, many radio galaxies are

strong submillimeter emitters (e.g., Archibald et al. 2001; Greve et al. 2006) and would qualify as SMGs irrespective of their strong radio emission.

5.3. Mid-IR Luminosities

The rest-frame 5 μm monochromatic luminosities presented in Table 4 are generally all above $10^{11} L_{\odot}$. In Figure 10 we show the distribution of the 5 μm luminosities with redshift. The solid symbols and arrows indicate the 21 HzRGs with MIPS detections and the five HzRGs with MIPS upper limits. The open symbols indicate the 13 HzRGs with IRS observations, but no MIPS observations in which the IRS band is close to rest-frame 5 μm . These IRS-derived luminosities are calculated directly from the 16 μm flux densities and thus do not account for the shape of the SED or the related offset between rest-frame 5 μm and the rest-frame wavelength probed by the 16 μm observations. The uncertainty on the IRS-derived rest-frame 5 μm luminosities is estimated to be $\lesssim 50\%$.

The high luminosities, $L_{5\mu\text{m}} \gtrsim 10^{11} L_{\odot}$, in Figure 10 imply that the HzRGs are reradiating a substantial amount of energy, most likely reprocessed emission from the obscured AGN heating the surrounding dust. The implied total (5–1000 μm) IR

FIG. 6—*Continued*

luminosities will be greater than the mid-IR luminosities presented here and hence most of these HzRGs would be classified as LIRGs ($L_{5-1000\ \mu\text{m}} > 10^{11} L_{\odot}$), or in many cases as ULIRGs ($L_{5-1000\ \mu\text{m}} > 10^{12} L_{\odot}$) had they been initially identified with no knowledge of their radio properties. These luminosities cover a similar range as those found by Ogle et al. (2006) for a sample of quasars and radio galaxies from the 3CRR catalog: $\nu L_{\nu}(\text{rest } 15\ \mu\text{m}) = 10^{44}-10^{46}\ \text{ergs s}^{-1}$. Luminosities this high confirm that powerful radio galaxies harbor “hidden quasars,” i.e., supermassive black holes accreting near the Eddington limit. A few sources have lower luminosities, classified by Ogle et al. (2006) as being in the mid-IR “weak” regime, $\nu L_{\nu}(\text{rest } 15\ \mu\text{m}) < 10^{44}\ \text{ergs s}^{-1}$, approximately equivalent to $\nu L_{\nu}(\text{rest } 5\ \mu\text{m}) < 10^{11} L_{\odot}$, indicating that they probably have lower accretion rates and are possibly nonthermal, jet-dominated sources.

The alternate explanation for these high mid-IR luminosities, star formation, is unlikely. Despite the high inferred star formation rates from the submillimeter observations (Archibald et al. 2001; Reuland et al. 2003), $\geq 500 M_{\odot}\ \text{yr}^{-1}$ for the $\sim 30\%$ detected and $\leq 500 M_{\odot}\ \text{yr}^{-1}$ for the nondetections, the star formation is widely scattered as seen in the rest-frame UV/optical images, which show widely distributed morphologies (McCarthy et al. 1987; Best et al. 1996; Zirm et al. 2003; Miley et al. 2006). Hence,

the star formation is unlikely to be dense enough to reach temperatures where it would dominate at rest frame $5\ \mu\text{m}$.

5.4. Near- to Mid-IR Luminosity Ratio

Figure 11 presents the stellar near-IR to total mid-IR ($L_{\text{H}}^{\text{stel}}/L_{5\ \mu\text{m}}^{\text{tot}}$) rest-frame luminosity ratio plotted against both redshift and 3 GHz luminosity. The ratios range from ~ 0.1 to ~ 6 , and we find that the near- to mid-IR luminosity ratio gradually decreases with both increasing redshift and with increasing radio luminosity. If, as discussed earlier, the mid-IR luminosities are indicators of the power of the AGN (i.e., the AGN accretion rate at the epoch of observation), then for a given host stellar mass, the accretion rate apparently declines at lower redshift and lower radio power. This correlation suggests evolution with redshift, but it may also be due to selection: our mid-IR luminosities are based on the $24\ \mu\text{m}$ detections, which are fewer at higher redshift. The trend with radio power is perhaps more interesting, showing that HzRGs with more luminous radio emission are also accreting at a higher rates (for a given stellar mass). This result is also consistent with the radio luminosity–emission line luminosity correlation (Willott et al. 1999). This trend with redshift is probably also related to the slight trend, albeit with a large scatter, when directly comparing the mid-IR to radio luminosity (see Fig. 12),

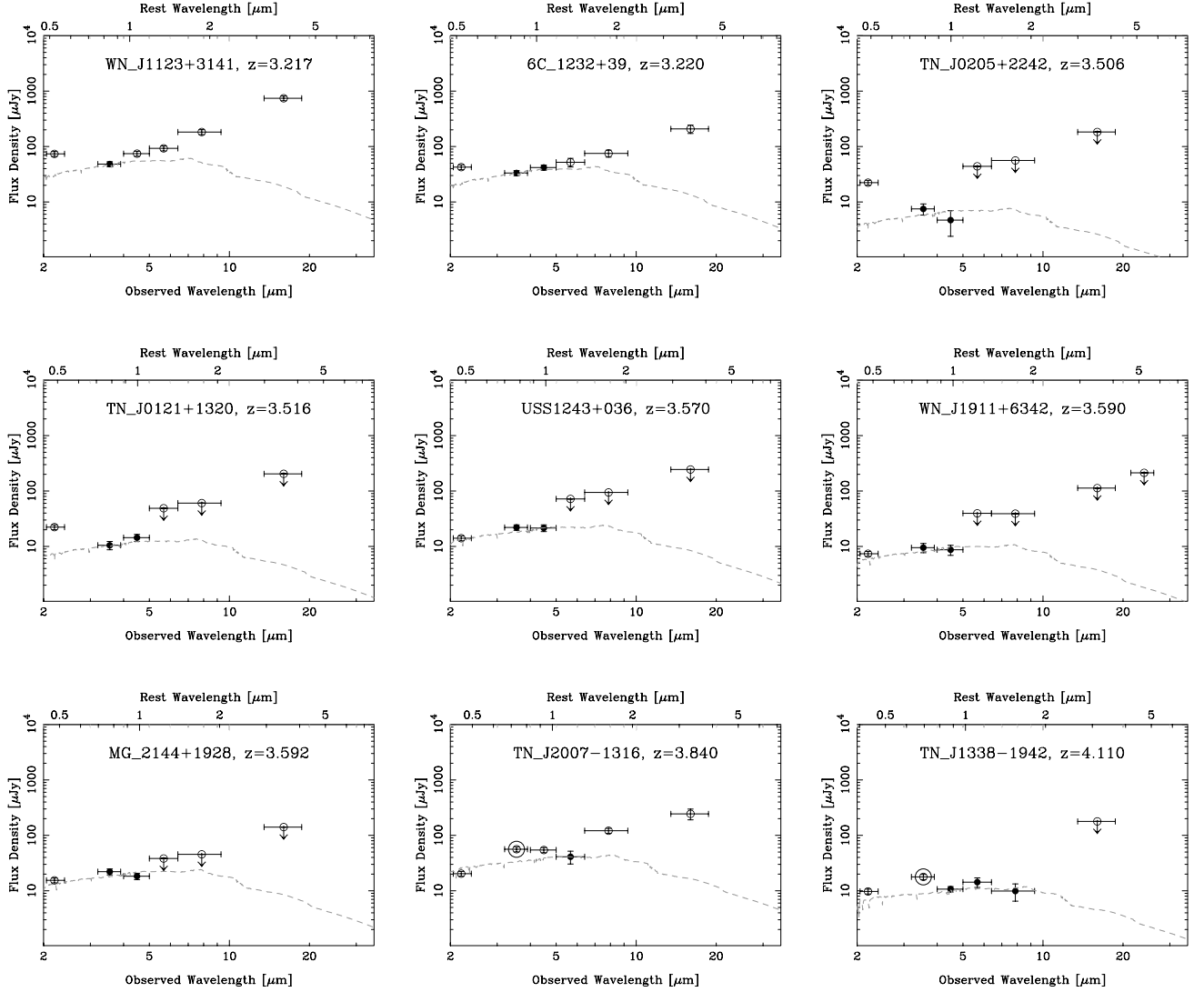


FIG. 6—Continued

although that trend is possibly due to the scaling of luminosities with distance.

6. PHOTOMETRIC STELLAR MASSES

The stellar luminosities shown in Figure 9 are converted to masses using the mass-to-light ratios¹⁸ derived from the PÉGASE.2 early-type galaxy model with $z_{\text{form}} = 10$ described in § 4.1 and are presented in Figure 13. The plotted errors are from the SED fitting of the luminosity; systematic errors to the stellar masses are discussed in § 6.3. Hence, we show that the stellar masses of the hosts of radio galaxies generally have masses distributed between 10^{11} and $10^{11.5} M_{\odot}$ with remarkable little scatter across the redshift range of $1 \leq z \leq 4$. The one HzRG with larger uncertainty at $z = 5.2$ suggests that this trend may hold to higher redshifts still with the implication that this source had to have formed early and quickly. Given that the lifetimes of radio galaxies are short, 10–100 Myr, these sources are likely to be rep-

resentative of a larger population of massive galaxies at these redshifts. Massive galaxies are now being found in great numbers across $1 \leq z \leq 3$ (e.g., Labbé et al. 2005; Papovich et al. 2006; van Dokkum et al. 2006).

We compare our HzRG sample to SMGs studied by Borys et al. (2005) (Fig. 13, *red crosses*). HzRGs and SMGs are among the most massive objects over this redshift range, showing that both classes of galaxy probe the most massive galaxies in the high-redshift universe, although we note that HzRGs are much rarer beasts. Borys et al. (2005) studies 13 SMGs identified in the GOODS survey. For comparison, the most luminous radio source known in the GOODS survey is VLA J123642+621331, a 470 μJy source at $z = 4.24$ identified by (Waddington et al. 1999). With $L_{3\text{ GHz}} \sim 10^{25} \text{ W Hz}^{-1}$, the radio emission from this galaxy is most likely coming from an AGN, not star formation, as suggested by European VLBI Network observations (Garrett et al. 2001), which show the source to be unresolved. Nevertheless, its radio power does not qualify it as a HzRG according to our selection criteria defined in § 2.

6.1. Radio Power Dependence on Stellar Mass

Figure 14 presents the derived stellar masses plotted against rest-frame 3 GHz radio luminosity. The small dynamic range of

¹⁸ The modeled mass-to-light ratios include the mass of *all* material that has gone through star formation. It thus represents the integrated star formation history and includes stars, as well as substellar objects and compact poststellar relics such as white dwarfs, neutron stars, and black holes, but *not* the gas that is recycled to the ISM. Stars dominate the rest-frame near-IR SED.

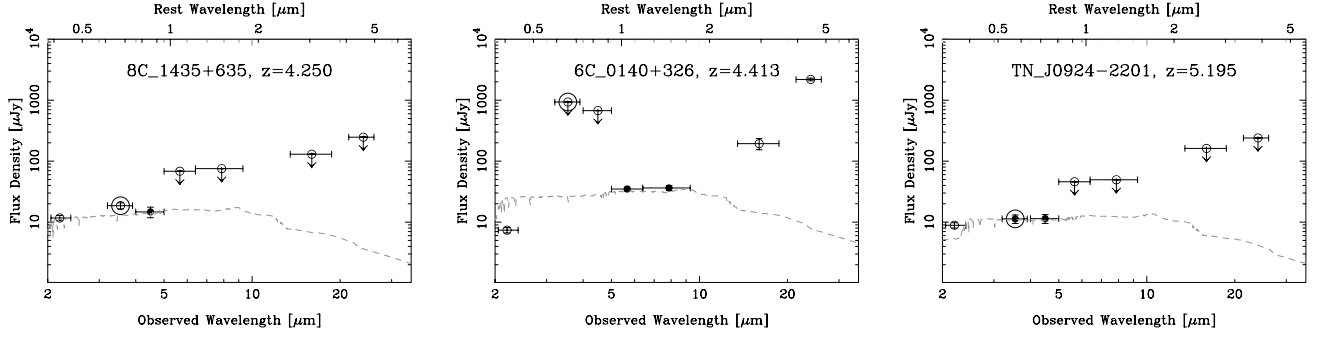


FIG. 6—Continued

the stellar masses combined with their relatively large uncertainties makes the formal determination of any correlation difficult, but a weak correlation is visually apparent. A proper statistical survival analysis that accounts for the multiple upper limits finds that the Cox hazard probability is only 0.5, meaning there is only a 50% chance that stellar mass correlates with radio luminosity for our sample. The detection of a correlation, showing that more powerful radio sources are hosted by more massive galaxies, would not be surprising, and is in fact expected if the M - σ relation holds to high redshift and all HzRGs have similar efficiency rates or Eddington ratios. Previous work, inferring stellar masses from the *observed* near-IR flux rather than the *rest-frame* near-IR luminosity, has suggested this correlation in the past (Eales et al. 1997; Best et al. 1998; Jarvis et al. 2001; De Breuck et al. 2002; Willott et al. 2003).

6.2. Comparisons with More Detailed Modeling

As mentioned earlier, several HzRGs from our sample have already been the subject of detailed studies that included *Spitzer* observations and determined host stellar masses. These studies have generally used more extensive photometry for the modeling, including optical and near-IR data, and have used more complicated models to determine the host stellar masses. We review the results of more detailed modeling here; in brief, allowing for different choices of IMF, the simplistic modeling presented here is consistent with the more detailed modeling.

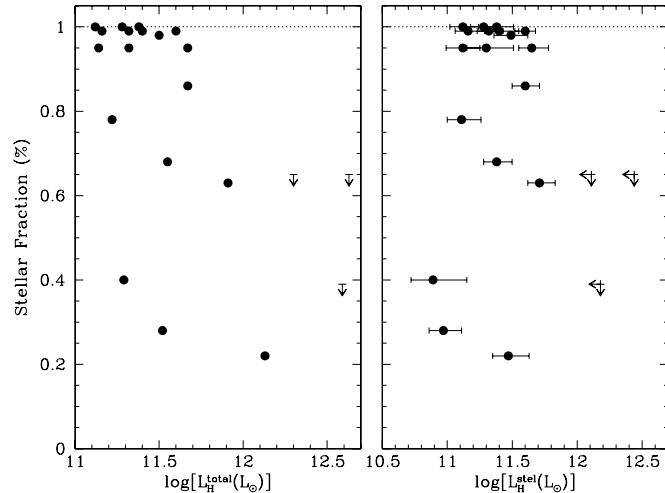


FIG. 7.— Fraction of the HzRG rest-frame H -band luminosity that is modeled as stellar, plotted as a function of total H -band luminosity and stellar H -band luminosity. The stellar fraction appears independent of the stellar near-IR luminosity but is inversely related to the total near-IR luminosity. This implies that the underlying hosts constitute a homogeneous, similar stellar mass population, but with varying AGN contributions to their observed total near-IR luminosities.

MRC 2104–242 ($z = 2.491$) was analyzed in detail by Villar-Martin et al. (2006), who found a stellar mass of $(5 \pm 2) \times 10^{11} M_{\odot}$, $E(B - V) = 0.4$, and an age of 1.8 Gyr. This result is consistent with the work here where we find a mass of $1.6^{+1.6}_{-0.8} \times 10^{11} M_{\odot}$. Our work assumes no extinction, and $z_{\text{form}} = 10$ corresponds to an age of 2.1 Gyr for the redshift of this HzRG. Much of the difference can be attributed to the Salpeter (1955) IMF adopted by Villar-Martin et al. (2006), which yields a mass-to-light ratio systematically higher by a factor of $\sim 40\%$ compared to the Kroupa (2001) IMF adopted here. Taking this choice into account, the derived masses are within 1σ of each other, which is rather encouraging given the increased sophistication of the stellar modeling in Villar-Martin et al. (2006), as well as their inclusion of near-IR data from the ground and *HST*.

LBDS 53W091 ($z = 1.552$) was studied by Stern et al. (2006) and, as discussed earlier, is (proto-) typical of the old, evolved class of extremely red objects. Using the Salpeter (1955) IMF, Stern et al. (2006) find a stellar mass of $\sim 3 \times 10^{11} M_{\odot}$ and an age of 3.5–4 Gyr. Accounting for the difference in IMF, this result is consistent with the masses presented here, $\sim 1.6 \times 10^{11} M_{\odot}$. The ages of the LBDS galaxies imply a redshift of formation $z_{\text{form}} \sim 9$, similar to our $z_{\text{form}} = 10$.

The full radio to X-ray SED of 4C 23.56 ($z = 2.483$) is presented in C. De Breuck et al. (2007, in preparation), the first time such data has been presented for a radio galaxy above $z = 2$. A full SED decomposition of the AGN and stellar emission (such as scatter quasar light, emission lines and nebular continuum) is performed. With a Salpeter IMF and no extinction, they derive a

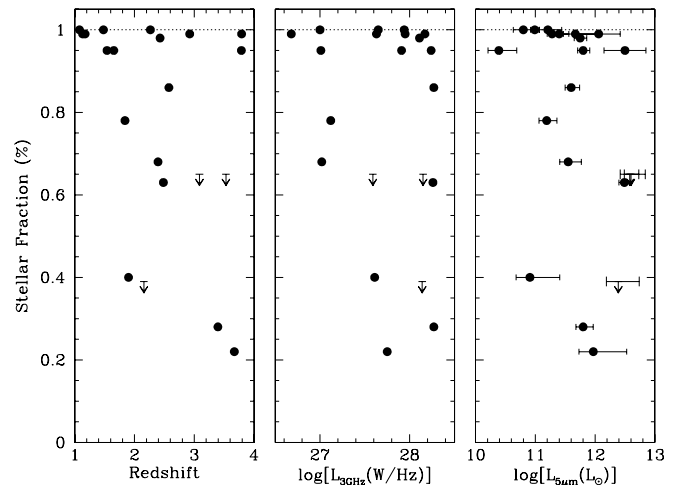


FIG. 8.— Fraction of the HzRG rest-frame H -band luminosity that is modeled as stellar, plotted as a function of (1) redshift, (2) rest-frame 3 GHz radio power, and (3) rest-frame $5 \mu\text{m}$ luminosity. Only the 21 HzRGs with MIPS detections are plotted. No correlations are evident.

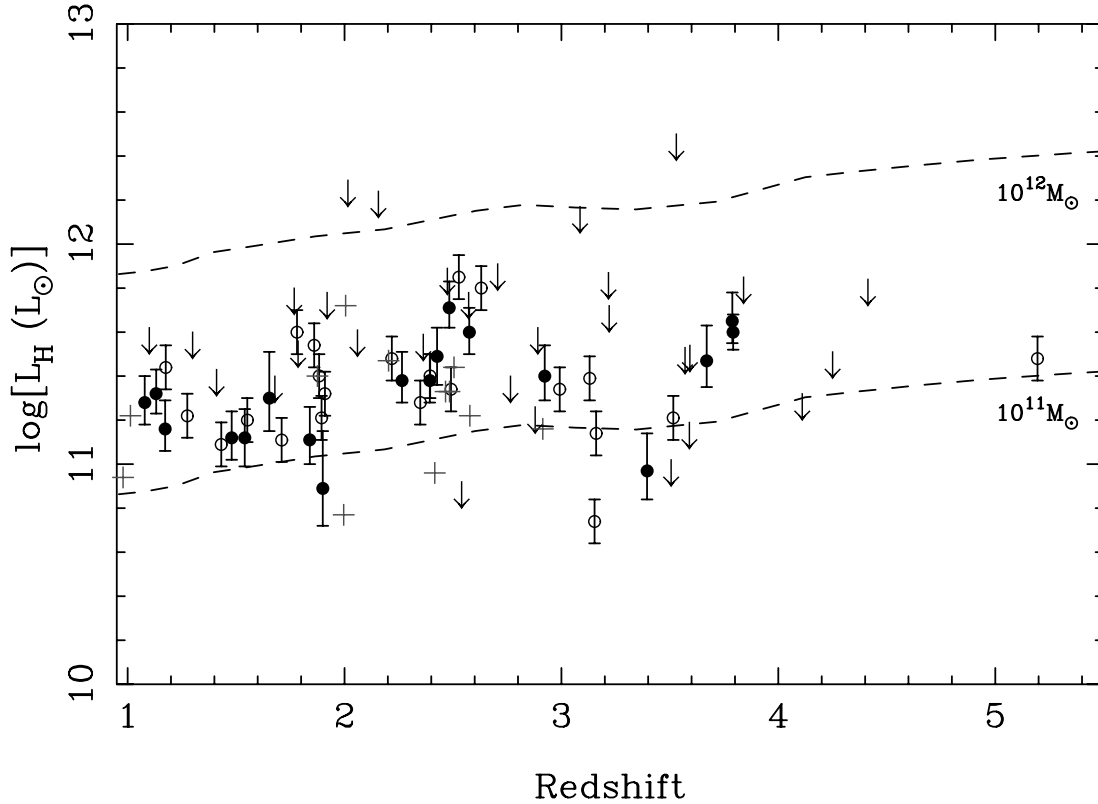


FIG. 9.—Rest-frame H -band stellar luminosity vs. redshift for the *Spitzer* HzRG sample, derived from the best-fit models to the multiband photometry. Solid circles indicate those luminosities derived from HzRGs with MIPS detections, while open circles are luminosities derived from HzRGs without MIPS detections. Those radio galaxies where only a maximum fit of the stellar SED was possible have upper limits, indicated by arrows. The dashed lines represent the luminosities of elliptical galaxies with $z_{\text{form}} = 10$ taken from the PÉGASe.2 models and normalized to 10^{11} and $10^{12} M_{\odot}$. Crosses mark the stellar luminosity of submillimeter galaxies from Borys et al. (2005), rederived in the same fashion as our HzRG sample. [See the electronic edition of the Supplement for a color version of this figure.]

stellar mass of $5.1^{+1.6}_{-2.1} \times 10^{11} M_{\odot}$. Again, allowing for the different choice of IMF, this result is consistent within 1σ of the results here, $3.9^{+1.2}_{-0.7} \times 10^{11} M_{\odot}$.

These comparisons give us confidence that although the SED modeling we adopt is somewhat simplistic, the derived stellar masses appear to be accurate within the uncertainties inherent to the enterprise.

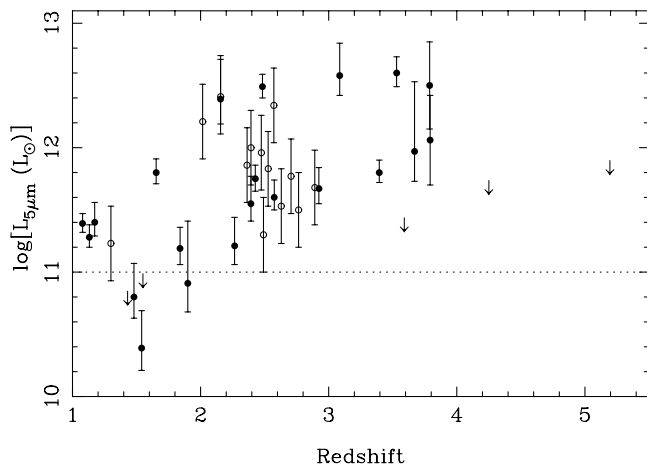


FIG. 10.—Rest $5 \mu\text{m}$ monochromatic luminosity vs. redshift. Filled symbols indicate sources observed with MIPS; open symbols indicate sources without MIPS observations but observed with IRS. Dotted line represents the divide between mid-IR “strong” and mid-IR “weak” AGNs, as defined by Ogle et al. (2006).

6.3. Systematic Effects on the Stellar Masses

Deriving stellar masses of high-redshift galaxies ($z \gtrsim 1$) has become widespread in recent years with the advent of deep near- and mid-IR extragalactic surveys (e.g., Shapley et al. 2003; Labbé et al. 2005; Rettura et al. 2006; L. A. Moustakas et al. 2007, in preparation). *Photometric* masses, as derived here, are subject to several systematic uncertainties. However, “relative” masses can be derived with less uncertainty (e.g., Dickinson et al. 2003). We now briefly discuss some of the systematic effects inherent to the stellar masses derived here. This analysis will be particularly important for future comparison of our results with other samples.

6.3.1. IMF

The IMF remains one of the largest uncertainties when modeling the SED of a galaxy. There have been several updates to the classical Salpeter (1955) IMF recently (e.g., Kroupa 2001; Chabrier 2003; etc.). Even these, however, are largely based on local stars within our own Galaxy and hence suffer uncertainties at the low-mass end and for extreme metallicities (high and low). We have chosen to use the Kroupa (2001) IMF here. However, our results would not be very different ($<2\%$) if we used the Chabrier (2003) IMF. Had we used the classical Salpeter (1955) IMF, our stellar masses would increase systematically by 40%, independent of our choice of z_{form} .

6.3.2. Formation Redshift

We have assumed a uniform formation redshift, $z_{\text{form}} = 10$, in the current analysis. Eyles et al. (2006) find a range of $z_{\text{form}} = 7\text{--}14$ for i' -band dropouts at $z \sim 6$ in the GOODS fields for

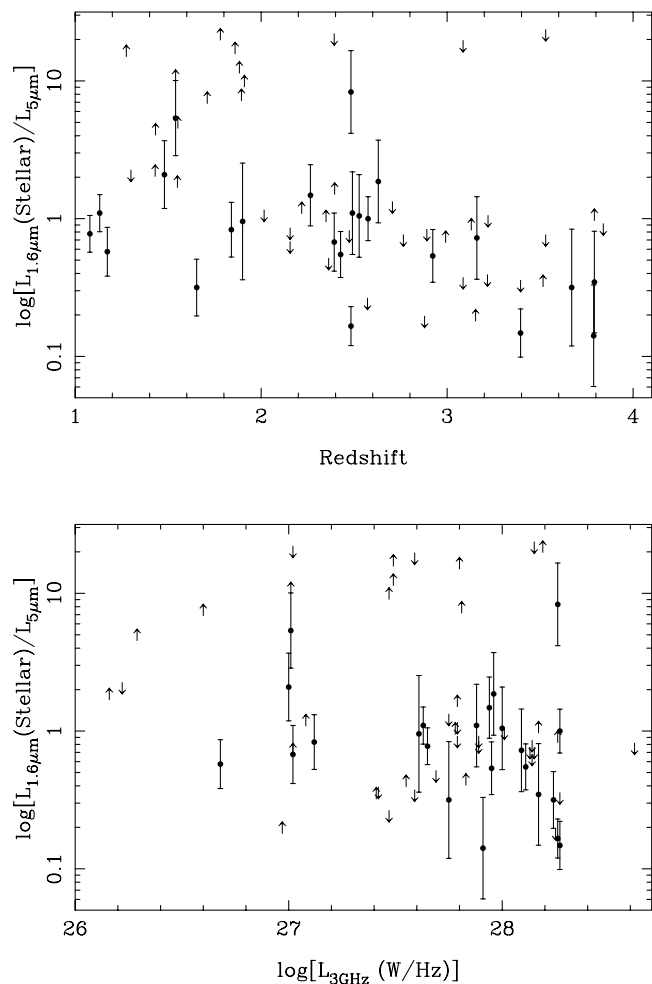


FIG. 11.—Ratio of rest-frame stellar near-IR (H -band) luminosity to total mid-IR ($5\ \mu\text{m}$) luminosity against redshift (*top*) and 3 GHz luminosity (*bottom*). This ratio appears to strongly correlate with both redshift and radio luminosity, although both correlations are probably due to the loose correlation of the $5\ \mu\text{m}$ luminosity with both redshift and radio luminosity.

galaxies. These distant galaxies are our best-studied examples of galaxies at $6 \lesssim z \lesssim 7$ and hence are our best (only) candidates for the parent populations to HzRGs. This range of formation redshifts corresponds to 0.16 Gyr earlier or 0.3 Gyr later than $z = 10$ when the universe was only ~ 1 Gyr old. Assuming the full range of z_{form} from Eyles et al. (2006) changes the mass by $\pm 17\%$ for a Kroupa (2001) IMF and $\pm 8\%$ for a Salpeter (1955) IMF. The change is such that the stellar mass decreases with a later formation redshift and vice versa.

6.3.3. Extinction

No internal galactic extinction is considered here. However, $\sim 50\%$ of the HzRGs have submillimeter detections, implying substantial dust content, although the dust distribution need not heavily obscure the old stellar population observed at rest-frame near-IR wavelengths. To obtain a 20% underestimation of the stellar mass from the rest-frame H -band luminosity requires an $A_V > 1.17$ assuming a Calzetti et al. (1994) extinction curve.

6.3.4. Starburst Component

These stellar mass estimates do not include the possible contribution of young stellar populations, which would lead to an over estimation of the stellar mass. If we include a 10% by mass starburst component, starting 200 Myr before the observed red-

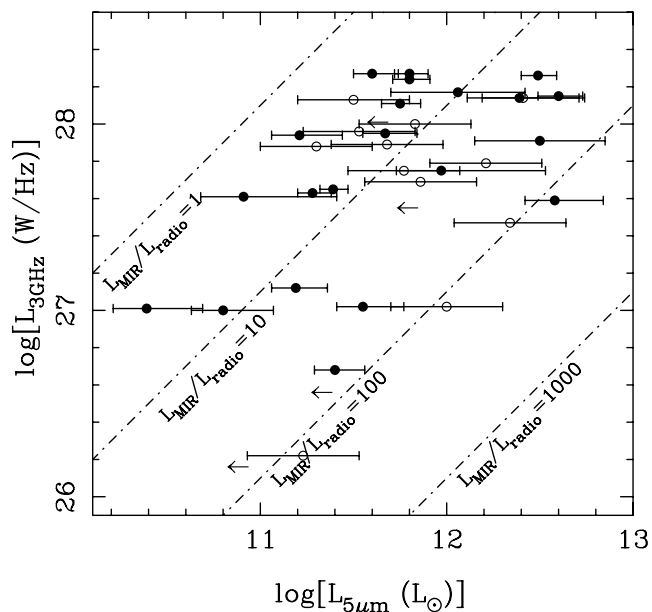


FIG. 12.—Rest $5\ \mu\text{m}$ monochromatic luminosities vs. rest 3 GHz radio luminosities showing a slight correlation potentially due to distance effects, or more likely demonstrating the both mid-IR and radio luminosity trace AGN power and that the scatter is induced by the time delay of jets powering the lobes after a change in AGN power.

shift, we find that, while the SED at rest-frame near-IR does not change significantly, the mass-to-light ratio does decrease by 10%–20% at H band (see Fig. 2). Redoing our analysis again with this younger component results in nearly identical H -band luminosities as before, but a $\lesssim 20\%$ decrease in stellar mass. We note that despite several sources in our sample having submillimeter detections, it is not thought that on-going star formation constitutes as much as 10% by mass for such systems.

Deep rest-frame UV spectropolarimetry of nine optically bright star-forming HzRGs by Vernet et al. (2001) finds only one object with a substantial contribution from a population of young stars. Hence, we conclude that there may be a mild systematic overestimation of the stellar mass, but this uncertainty is likely less significant than other uncertainties discussed above, such as the choice of the IMF in the modeling.

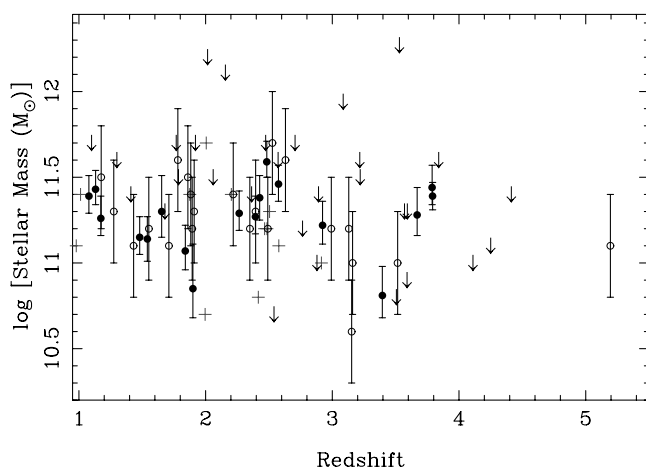


FIG. 13.—Stellar mass in solar units plotted against redshift for the 69 *Spitzer* HzRGs. Symbols are as in Fig. 9. [See the electronic edition of the Supplement for a color version of this figure.]

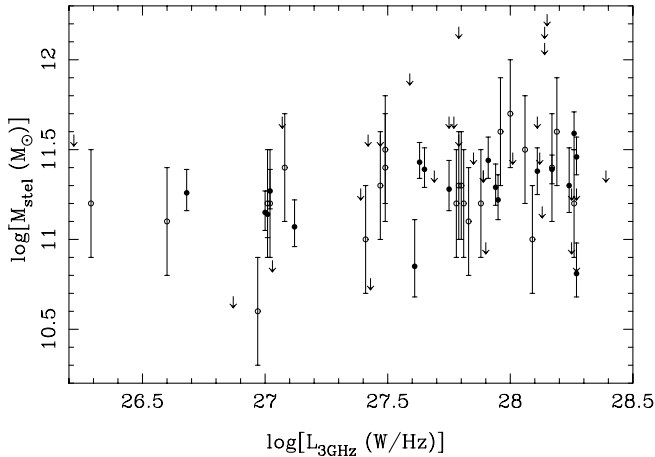


FIG. 14.—Stellar mass against rest-frame 3 GHz luminosity. There is evidence of a slight trend, such that the most massive galaxies host more powerful radio sources, however, accounting for the large number of upper limits in the plot, a formal survival analysis shows only a 50% chance of the two observables being correlated. Deeper data and better coverage with the longer wavelength *Spitzer* cameras would show conclusively whether or not this correlation exists.

6.3.5. TP-AGB Stars

Maraston (2005) has argued that the thermally pulsing asymptotic giant branch (TP-AGB) phase in the evolution of a simple stellar population is not properly considered in other spectral evolution synthesis codes (e.g., PÉGASE and Bruzual & Charlot 2003), and hence analysis using these models overpredicts the near-IR mass-to-light ratio for galaxy ages $\lesssim 1$ Gyr. For our choice of z_{form} , this age corresponds to galaxies at $3 \lesssim z \lesssim 4$. We emphasize that the PÉGASE models *do* incorporate the TP-AGB phase, just in a different manner than the Maraston (2005) models. If this TP-AGB phase is indeed an issue, it is most likely to only affect the highest redshift (and hence youngest) sources in our sample by decreasing their stellar mass by $\lesssim 30\%$. As we have seen in § 6.3.4, an unaccounted starburst leads to an overestimation of the stellar mass. Use of the model from Maraston (2005) would hence increase this overestimate to about 30%, which is on par with the uncertainty due to all the other systematics.

7. DISCUSSION AND CONCLUSIONS

We have performed a comprehensive infrared survey of 69 HzRGs above $z = 1$, the first time such galaxies have been detected in the rest-frame near-IR and mid-IR. This work presents the largest sample of confirmed type 2 quasars to be systematically studied with *Spitzer*. As expected, they predominantly reside in the IRAC color-color space dominated by type 1 AGNs found empirically by Lacy et al. (2004) and Stern et al. (2005) and theoretically by Sajina et al. (2005).

We model the rest-frame near to mid-IR SEDs derived from our broad-band IRAC, IRS, and MIPS imaging. We use a toy model comprised of thermal BBs to represent the emission at longer wavelengths presumably due to dust, and the PÉGASE code to model the stellar component. Our analysis yields total near-IR (H band) and mid-IR ($5 \mu\text{m}$) rest-frame luminosities, and we deconvolve the stellar and AGN contributions at H band. The scatter of stellar H -band luminosities is lower than that for the total H -band luminosities, and we find the HzRGs with lower stellar fractions tend to have higher rest-frame H -band total luminosities, although this trend is weak. When H -band luminosities are corrected for AGN contribution, they show no correlation with stel-

lar fraction. In addition, the stellar fraction is not found to correlate with redshift, radio luminosity, or mid-IR luminosity. These results are consistent with orientation-driven models of AGN unification.

We find that the H -band stellar luminosities are consistent with stellar masses of 10^{11} – $10^{12} M_{\odot}$, comparable with the masses of local massive radio galaxies (McCarthy 1993; Jarvis et al. 2001; Willott et al. 2003). This conversion of luminosity to mass assumes a dust-free, passively evolving elliptical formed at $z = 10$ with no recent episodes of star-formation. We discuss these effects and other systematics and conclude that our findings are robust at the level of $\approx 10\%$ – 20% . We also note that effects can act to either increase the inferred mass (the presence of dust) or to decrease it (recent star-burst activity). So multiple effects may cancel out, thus most likely simply increasing the scatter in the estimated stellar masses.

The derived stellar masses average $10^{11.4} M_{\odot}$ across $z = 1$ – 4 with a scatter less than 50%. This scatter is remarkably small, suggesting that the tightness of the observed K - z relation at $z > 1$ is due to the intrinsic homogeneity of the HzRG population. The increase in the scatter from $z < 1$ to $z > 1$ can largely be attributed to the K -band being affected by emission lines, scattered light from the AGN (e.g., C. De Breuck et al. 2007, in preparation), and, potentially, young stellar populations. The scatter in the observed H -band luminosities can be explained by varying contributions from AGN-heated dust entering the IRAC bands.

These masses, while very high, are not uncommon at these redshifts. Much work has been done recently to detect massive, $M > 10^{11} M_{\odot}$, galaxies at high redshifts (e.g., Labbé et al. 2005; Papovich et al. 2006; van Dokkum et al. 2006). Densities of approximately one $M > 10^{11} M_{\odot}$ galaxy per square arcmin are found in the redshift range $2 \lesssim z \lesssim 3$ (Papovich et al. 2006; van Dokkum et al. 2006). Our survey targeted a sample of known sources from the literature, derived from multiple radio surveys. As such, we are ill posed to address space densities from the current work. However, we note that our adopted definition of a HzRG ($z > 1$ and $L_{3 \text{ GHz}} > 10^{26} \text{ W Hz}^{-1}$) implies that large area surveys such as the Faint Images of the Radio Sky at Twenty-centimeters (FIRST; Becker et al. 1995) have already detected all HzRGs at $1 < z \lesssim 3$, although the vast majority lack spectroscopic observations thus far. We can therefore constrain the surface density of HzRGs to be less than $< 100 \text{ deg}^{-2}$, which is significantly lower than the surface density of optically and near-IR selected massive galaxies. This low surface density is most likely due to the short lifetimes (10–100 Myr) and low duty cycles of the most powerful radio sources, even if the every massive galaxy were to go through a radio-luminous phase.

We find a slight trend that the galaxies with the higher stellar masses host the more powerful radio sources, a trend suggested by other authors (McCarthy 1993; Jarvis et al. 2001; Willott et al. 2003). However, a full survival analysis taking proper account of upper limits finds this correlation has only a 50% chance of being correct. The correlation is expected if the M - σ relation holds to high redshift and HzRGs all accrete at comparable Eddington ratios.

Most of the HzRG mid-IR luminosities are above $10^{11} L_{\odot}$, implying even higher total IR luminosities. These LIRG and ULIRG-like luminosities are due to reprocessed radiation from gas and dust obscuring a highly accreting AGN. Rest-frame mid-IR luminosity ($\lambda_0 \sim 5 \mu\text{m}$) may be a good, independent indicator of AGN activity. Comparison with traditional AGN indicators at other wavelengths is currently underway (X-ray: D. Alexander et al. 2007, in preparation; radio: N. Seymour et al. 2007, in preparation).

We would like to thank the referee for the constructive comments provided on the clarification of this paper. N. S. and D. S. thank ESO for generous hospitality on several occasions over the last few years. We thank Dave Frayer and Ranga-Ram Chary for advice on reducing the MIPS data and the IRAC instrument team for allowing publication of GTO data on 4C 41.17 and 6C 0140+326.

This work is based on observations made with the *Spitzer Space Telescope*, which is operated by the Jet Propulsion Laboratory, California Institute of Technology under a contract with

NASA. Support for this work was provided by NASA through an award issued by JPL/Caltech. The work by W. v. B. was performed under the auspices of the US Department of Energy, National Nuclear Security Administration by the University of California, Lawrence Livermore National Laboratory under contract W-7405-Eng-48. W. v. B. also acknowledges support for radio galaxy studies at UC Merced, including the work reported here, with the *Spitzer Space Telescope* via NASA grants SST 1264353, 1265551, 1279182, and 1281587.

APPENDIX

NOTES ON INDIVIDUAL SOURCES

Here we provide individual comments on selected HzRGs. The SED fitting is presented in Figure 5 (20 sources with MIPS detections) and Figure 6 (50 sources without MIPS detection), arranged in order of increasing redshift.

3C 65 ($z = 1.176$).—This HzRG was observed in only two bands due to an astrometric error in NED, which we have since had corrected.

3C 294 ($z = 1.786$).—While this radio galaxy is detected in all IRAC bands, the photometry is severely affected by a bright star 8'' to the east by northeast. This bright star has allowed detailed adaptive optics imaging of this object (e.g., Quirrenbach et al. 2001; Steinbring et al. 2002).

B3 J2330+3927 ($z = 3.086$).—This HzRG is one of two sources consistent with an AGN power law dominating the entire optical to mid-IR emission. We therefore can only provide an upper limit to the stellar mass. Although optical and near-IR spectroscopy (De Breuck et al. 2003) show a classical type 2 AGN spectrum, Pérez-Torres & De Breuck (2005) found that the radio morphology is more consistent with a type 1 AGN. The latter would be in agreement with the high contribution from hot AGN light seen in the near- to mid-IR SED.

MRC 0316–257 ($z = 3.131$).—Due to an error at the time of proposal submission, the source observed with IRAC was MRC 0316–257B (Le Fèvre et al. 1996), a spectroscopically confirmed $z = 3.118$ AGN, 71'' from MRC 0316–257. We used the deeper Cycle 1 GO data (Program ID 3482, PI van Breugel), but no IRS 16 μm data are available for the $z > 2$ radio galaxy.

TX J1908+7220 ($z = 3.53$).—This HzRG is the second of two sources consistent with an AGN power law dominating the entire optical to mid-IR emission. We therefore can only provide an upper limit to the stellar mass.

TN J1338–1942 ($z = 4.11$).—This HzRG is the fourth highest redshift source in our sample (De Breuck et al. 1999). Although the 3.6 μm IRAC band is likely to be contaminated by $\text{H}\alpha$, the remaining bands are consistent with a stellar SED. The low 8.0 μm flux ensures that any hot dust contamination will be small.

8C 1435+635 ($z = 4.25$).—This HzRG is the third highest redshift source in our sample (Lacy et al. 1994). The stellar mass estimate is based on the 4.5 μm IRAC detection only, as the 3.6 μm band is likely to be contaminated by $\text{H}\alpha$ emission.

6C 0140+326 ($z = 4.41$).—This HzRG is the second most distant galaxy and is masked by a bright, foreground galaxy in IRAC channels 1 and 2, thus rendering source extraction at these wavelengths infeasible.

TN J0924–2201 ($z = 5.19$).—This HzRG is the most distant radio galaxy in our sample (van Breugel et al. 1999). It is detected only at 3.6 and 4.5 μm . Deeper IRAC data have been obtained (Program ID 20749; PI: W. Zheng), but these data were not public yet at the time of writing (2006 December).

REFERENCES

- Antonucci, R. 1993, *ARA&A*, 31, 473
 Archibald, E. N., Dunlop, J. S., Hughes, D. H., Rawlings, S., Eales, S. A., & Ivison, R. J. 2001, *MNRAS*, 323, 417
 Athreya, R. M., Kapahi, V. K., McCarthy, P. J., & van Breugel, W. 1997, *MNRAS*, 289, 525
 Barthel, P. D. 1989, *ApJ*, 336, 606
 Becker, R. H., White, R. L., & Helfand, D. J. 1995, *ApJ*, 450, 559
 Bennett, A. S. 1962, *MmRAS*, 68, 163
 Bennett, C. L., Lawrence, C. R., Burke, B. F., Hewitt, J. N., & Mahoney, J. 1986, *ApJS*, 61, 1
 Bertin, E., & Arnouts, S. 1996, *A&AS*, 117, 393
 Best, P. N., Longair, M. S., & Röttgering, H. J. A. 1996, *MNRAS*, 280, L9
 ———. 1998, *MNRAS*, 295, 549
 Blandford, R., & Payne, D. 1982, *MNRAS*, 199, 883
 Blundell, K. M., Rawlings, S., Eales, S. A., Taylor, G. B., & Bradley, A. D. 1998, *MNRAS*, 295, 265
 Borys, C., Chapman, S., Halpern, M., & Scott, D. 2003, *MNRAS*, 344, 385
 Borys, C., Smail, I., Chapman, S. C., Blain, A. W., Alexander, D. M., & Ivison, R. J. 2005, *ApJ*, 635, 853
 Broderick, J. W., De Breuck, C., Hunstead, R. W., & Seymour, N. 2007, *MNRAS*, 375, 1059
 Brookes, M. H., Best, P. N., Rengelink, R., & Röttgering, H. J. A. 2006, *MNRAS*, 366, 1265
 Bruzual, G., & Charlot, S. 2003, *MNRAS*, 344, 1000
 Calzetti, D., Kinney, A. L., & Storchi-Bergmann, T. 1994, *ApJ*, 429, 582
 Chabrier, G. 2003, *PASP*, 115, 763
 Chambers, K. C., Miley, G. K., van Breugel, W. J. M., Bremer, M. A. R., Huang, J.-S., & Trentham, N. A. 1996, *ApJS*, 106, 247
 Cleary, K., et al. 2007, *ApJ*, 660, 117
 Condon, J. J., Cotton, W. D., Greisen, E. W., Yin, Q. F., Perley, R. A., Perley, G. B., Taylor, G. B., & Broderick, J. J. 1998, *AJ*, 115, 1693
 De Breuck, C., van Breugel, W., Minniti, D., Miley, G., Röttgering, H., Stanford, S. A., & Carilli, C. 1999, *A&A*, 352, L51
 De Breuck, C., et al. 2001, *AJ*, 121, 1241
 ———. 2002, *AJ*, 123, 637
 ———. 2003, *A&A*, 401, 911
 Devriendt, J. E. G., Guiderdoni, B., & Sadat, R. 1999, *A&A*, 350, 381
 Dey, A., Cimatti, A., van Breugel, W., Antonucci, R., & Spinrad, H. 1996, *ApJ*, 465, 157
 Dey, A., & Spinrad, H. 1996, *ApJ*, 459, 133
 Dickinson, M., Papovich, C., Ferguson, H. C., & Budavári, T. 2003, *ApJ*, 587, 25
 Douglas, J. N., Bash, F. N., Bozayan, F. A., Torrence, G. W., & Wolfe, C. 1996, *AJ*, 111, 1945
 Eales, S., & Rawlings, S. 1996, *ApJ*, 460, 68
 Eales, S., Rawlings, S., Law-Green, D., Cotter, G., & Lacy, M. 1997, *MNRAS*, 291, 593
 Eyles, L., et al. 2006, *MNRAS*, 374, 910

- Fanaroff, B. L., & Riley, J. M. 1974, *MNRAS*, 167, 31
- Fazio, G. G., et al. 2004, *ApJS*, 154, 10
- Fioc, M., & Rocca-Volmerange, B. 1997, *A&A*, 326, 950
- Garrett, M. A., et al. 2001, *A&A*, 366, L5
- Granato, G. L., Danese, L., & Franceschini, A. 1997, *ApJ*, 486, 147
- Gregg, M. D., Becker, R. H., White, R. L., Helfand, D. J., McMahon, R. G., & Hook, I. M. 1996, *AJ*, 112, 407
- Greve, T. R., Ivison, R. J., & Stevens, J. A. 2006, *Astron. Nachr.*, 327, 208
- Haas, M., Siebenmorgen, R., Schulz, B., Krügel, E., & Chini, R. 2005, *A&A*, 442, L39
- Heckman, T. M., O'Dea, C. P., Baum, S. A., & Laurikainen, E. 1994, *ApJ*, 428, 65
- Houck, J. R., et al. 2004, *ApJS*, 154, 18
- Jarvis, M. J., Rawlings, S., Eales, S., Blundell, K. M., Bunker, A. J., Croft, S., McLure, R. J., & Willott, C. J. 2001, *MNRAS*, 326, 1585
- Kroupa, P. 2001, *MNRAS*, 322, 231
- Labbé, I., et al. 2005, *ApJ*, 624, L81
- Lacy, M., Rawlings, S., Hill, G. J., Bunker, A. J., Ridgway, S. E., & Stern, D. 1999, *MNRAS*, 308, 1096
- Lacy, M., et al. 1994, *MNRAS*, 271, 504
- . 2004, *ApJS*, 154, 166
- . 2005, *ApJS*, 161, 41
- . 2007, *AJ*, 133, 186
- Lawrence, C. R., Readhead, A. C. S., Moffet, A. T., & Birkinshaw, M. 1986, *ApJS*, 61, 105
- Le Borgne, D., & Rocca-Volmerange, B. 2002, *A&A*, 386, 446
- Le Fèvre, O., Deltorn, J. M., Crampton, D., & Dickinson, M. 1996, *ApJ*, 471, L11
- Lilly, S. J., & Longair, M. S. 1984, *MNRAS*, 211, 833
- Makovoz, D., & Khan, I. 2005, in *ASP Conf. Ser. 347, Astronomical Data Analysis Software and Systems XIV*, ed. P. Shopbell, M. Britton, & R. Ebert (San Francisco: ASP), 81
- Maraston, C. 2005, *MNRAS*, 362, 799
- Martinez-Sansigre, A., Rawlings, S., Lacy, M., Fadda, D., Marleau, F. R., Simpson, C., Willott, C. J., & Jarvis, M. J. 2005, *Nature*, 436, 666
- Matthews, T. A., Morgan, W. W., & Schmidt, M. 1964, *ApJ*, 140, 35
- McCarthy, P. J. 1993, *ARA&A*, 31, 639
- McCarthy, P. J., Baum, S. A., & Spinrad, H. 1996, *ApJS*, 106, 281
- McCarthy, P. J., van Breugel, W., Spinrad, H., & Djorgovski, S. 1987, *ApJ*, 321, L29
- Miley, G. K., et al. 2006, *ApJ*, 650, L29
- Miller, L., Peacock, J. A., & Mead, A. R. G. 1990, *MNRAS*, 244, 207
- Nenkova, M., Ivezić, Ž., & Elitzur, M. 2002, *ApJ*, 570, L9
- Nesvadba, N. P. H., Lehnert, M. D., Eisenhauer, F., Gilbert, A., Tecza, M., & Abuter, R. 2006, *ApJ*, 650, 693
- Norman, C., et al. 2002, *ApJ*, 571, 218
- Ogle, P., Whysong, D., & Antonucci, R. 2006, *ApJ*, 647, 161
- Papovich, C., et al. 2006, *ApJ*, 640, 92
- Pascarelle, S. M., Windhorst, R. A., Keel, W. C., & Odewahn, S. C. 1996, *Nature*, 383, 45
- Pentericci, L., et al. 2001, *ApJS*, 135, 63
- Pérez-Torres, M.-A., & De Breuck, C. 2005, *MNRAS*, 363, L41
- Pier, E. A., & Krolik, J. H. 1992, *ApJ*, 401, 99
- Polletta, M. d. C., et al. 2006, *ApJ*, 642, 673
- Quirrenbach, A., Roberts, J. E., Fidkowski, K., de Vries, W., & van Breugel, W. 2001, *ApJ*, 556, 108
- Rees, M. J. 1978, *Nature*, 275, 516
- Rengelink, R. B., Tang, Y., de Bruyn, A. G., Miley, G. K., Bremer, M. N., Roettgering, H. J. A., & Bremer, M. A. R. 1997, *A&AS*, 124, 259
- Rettura, A., et al. 2006, *A&A*, 458, 717
- Reuland, M., Röttgering, H., van Breugel, W., & De Breuck, C. 2004, *MNRAS*, 353, 377
- Reuland, M., et al. 2003, *ApJ*, 592, 755
- Richards, G. T., et al. 2006, *ApJS*, 166, 470
- Rieke, G. H., et al. 2004, *ApJS*, 154, 25
- Rocca-Volmerange, B., Le Borgne, D., De Breuck, C., Fioc, M., & Moy, E. 2004, *A&A*, 415, 931
- Rocca-Volmerange, B., & Remazeilles, M. 2005, *A&A*, 433, 73
- Röttgering, H. J. A., van Ojik, R., Chambers, K., van Breugel, W., & de Koff, S. 1997, *A&A*, 326, 505
- Sajina, A., Lacy, M., & Scott, D. 2005, *ApJ*, 621, 256
- Salpeter, E. E. 1955, *ApJ*, 121, 161
- Saripalli, L., Hunstead, R. W., Subrahmanyam, R., & Boyce, E. 2005, *AJ*, 130, 896
- Sawicki, M. 2002, *AJ*, 124, 3050
- Shapley, A. E., Steidel, C. C., Pettini, M., & Adelberger, K. L. 2003, *ApJ*, 588, 65
- Siebenmorgen, R., Freudling, W., Krügel, E., & Haas, M. 2004, *A&A*, 421, 129
- Songaila, A., Cowie, L. L., Hu, E. M., & Gardner, J. P. 1994, *ApJS*, 94, 461
- Spergel, D., et al. 2007, *ApJS*, 170, 377
- Spinrad, H., Djorgovski, S., Marr, J., & Aguilar, L. 1985, *PASP*, 97, 932
- Steinbring, E., Crampton, D., & Hutchings, J. B. 2002, *ApJ*, 569, 611
- Stern, D., Chary, R.-R., Eisenhardt, P. R. M., & Moustakas, L. A. 2006, *AJ*, 132, 1405
- Stern, D., Holden, B., Stanford, S. A., & Spinrad, H. 2003, *AJ*, 125, 2759
- Stern, D., & Spinrad, H. 1999, *PASP*, 111, 1475
- Stern, D., et al. 2002, *ApJ*, 568, 71
- . 2005, *ApJ*, 631, 163
- Teplitz, H. I., Charmandaris, V., Chary, R., Colbert, J. W., Armus, L., & Weedman, D. 2005, *ApJ*, 634, 128
- Treister, E., et al. 2004, *ApJ*, 616, 123
- Tremaine, S., et al. 2002, *ApJ*, 574, 740
- Urry, C. M., & Padovani, P. 1995, *PASP*, 107, 803
- van Breugel, W., De Breuck, C., Stanford, S. A., Stern, D., Röttgering, H., & Miley, G. 1999, *ApJ*, 518, L61
- van Breugel, W., Stanford, S. A., Spinrad, H., Stern, D., & Graham, J. R. 1998, *ApJ*, 502, 614
- van Dokkum, P. G., et al. 2006, *ApJ*, 638, L59
- Venemans, B. P., Kurk, J. D., Miley, G. K., & Röttgering, H. J. A. 2003, *NewA Rev.*, 47, 353
- Venemans, B. P., et al. 2002, *ApJ*, 569, L11
- . 2004, *A&A*, 424, L17
- . 2005, *A&A*, 431, 793
- . 2007, *A&A*, 461, 823
- Vernet, J., Fosbury, R. A. E., Villar-Martin, M., Cohen, M. H., Cimatti, A., di Serego Alighieri, S., & Goodrich, R. W. 2001, *A&A*, 366, 7
- Villar-Martin, M., et al. 2003, *MNRAS*, 346, 273
- . 2006, *MNRAS*, 366, L1
- Waddington, I., Windhorst, R. A., Cohen, S. H., Partridge, R. B., Spinrad, H., & Stern, D. 1999, *ApJ*, 526, L77
- Waddington, I., et al. 2002, *MNRAS*, 336, 1342
- Werner, M. W., et al. 2004, *ApJS*, 154, 1
- Willott, C. J., Rawlings, S., Blundell, K. M., & Lacy, M. 1999, *MNRAS*, 309, 1017
- Willott, C. J., Rawlings, S., Blundell, K. M., Lacy, M., & Eales, S. A. 2001, *MNRAS*, 322, 536
- Willott, C. J., Rawlings, S., Jarvis, M. J., & Blundell, K. M. 2003, *MNRAS*, 339, 173
- Zirm, A., Dickinson, M., & Dey, A. 2003, *ApJ*, 585, 90